A 17-Yr Climate Record of Environmental Parameters Derived from the Tropical Rainfall Measuring Mission (TRMM) Microwave Imager

FRANK J. WENTZ

Remote Sensing Systems, Santa Rosa, California

(Manuscript received 27 February 2015, in final form 22 May 2015)

ABSTRACT

The Tropical Rainfall Measuring Mission (TRMM) satellite began operating in December 1997 and was shut down on 8 April 2015. Over the oceans, the microwave (MW) sensor aboard TRMM measures sea surface temperature, wind speed, and rain rate as well as atmospheric columnar water vapor and cloud liquid water. Improved calibration methods are applied to the TRMM Microwave Imager (TMI), and a 17-yr climate record of these environmental parameters is produced so as to be consistent with the climate records from 13 other MW sensors. These TMI retrievals are validated relative to in situ observations over its 17-yr mission life. All indications point to TMI being an extremely stable sensor capable of providing satellite climate records of unprecedented length and accuracy.

1. Introduction

The microwave (MW) imaging radiometer on the Tropical Rainfall Measuring Mission (TRMM) satellite operated from December 1997 to the end of the TRMM mission on 8 April 2015. This sensor is called TMI for TRMM Microwave Imager. Over the oceans, TMI provides a full suite of environmental parameters including sea surface temperature (SST or T_S), wind speed (W), and rain rate (R), as well as atmospheric columnar water vapor (V) and cloud liquid water (L). The literature has many examples of the application of these satellite retrievals to climate research (Wentz and Schabel 2000; Wentz et al. 2000; Trenberth et al. 2005; Chelton and Wentz 2005; Mears et al. 2007; Wentz et al. 2007).

This paper describes the steps required to realize the full potential of TMI for climate applications. These include achieving proper geolocation, radio frequency interference (RFI) mitigation, and sensor calibration. With respect to calibration, the major challenge is to account for the slightly emissive TMI antenna, as discussed by Wentz et al. (2001). Some of the radiation received by TMI comes directly from the antenna and this component must be precisely removed. The results we show here indicate that TMI has been extremely stable over its 17-yr life.

An essential part of the analysis is to ensure the TMI calibration and the data processing algorithms are consistent with those used by Remote Sensing Systems (RSS) for the existing set of 13 MW sensors listed in Table 1. This table includes two MW scatterometers, for which the wind speed retrievals are consistent with the MW imagers. In 2010, RSS transitioned its Special Sensor Microwave Imager (SSM/I) processing from version 6 to version 7 (V7), which has become our common standard for all MW imagers (Wentz 2013). The V7 standard requires that the brightness temperature (T_B) calibration reference for all sensors be the Meissner and Wentz (2012) ocean radiative transfer model (RTM). All sensors listed in Table 1 have been consistently processed and are at the V7 calibration standard. With the completion of the analyses present here, TMI has become the most recent addition to this set of intercalibrated sensors.

2. TMI basic characteristics

The TMI sensor is well described in the literature (Kummerow et al. 1998), and here we provide a few details relevant to this paper. TMI is a conically scanning radiometer that operates at five frequencies: 10.65,

Denotes Open Access content.

Corresponding author address: Frank J. Wentz, Remote Sensing Systems, 444 Tenth Street, Santa Rosa, CA 95401.
E-mail: frank.wentz@remss.com.

DOI: 10.1175/JCLI-D-15-0155.1

TABLE 1. List of MW sensors processed to the V7 calibration standard (expansions of acronyms are available at http://www.ametsoc.org/PubsAcronymList; *GCOM-W1* is the *Global Change Observation Mission for Water 1* satellite).

Sensor	Short name	Operation period
SSM/I on DMSP *F08*	*F08*	Jul 1987–Dec 1991
SSM/I on DMSP *F10*	*F10*	Dec 1990–Nov 1997
SSM/I on DMSP *F11*	*F11*	Dec 1991–May 2000
SSM/I on DMSP *F13*	*F13*	May 1995–Nov 2009
SSM/I on DMSP *F14*	*F14*	May 1997–Aug 2008
SSM/I on DMSP *F15*	*F15*	Dec 1999–present
SSM/IS on DMSP *F16*	*F16*	Oct 2003–present
SSM/IS on DMSP *F17*	*F17*	Dec 2006–present
NRL WindSat on *Coriolis*	WindSat	Jan 2003–present
JAXA AMSR-E on *Aqua*	AMSR-E	May 2002–Oct 2011
JAXA AMSR-2 on *GCOM-W1*	AMSR-2	May 2012–present
NASA QuikScat scatterometer	QuikScat	Jun 1999–Nov 2009
EUMETSAT scatterometer on *MetOp-A*	ASCAT	Oct 2006–present

19.35, 21.25, 37.0, and 85.5 GHz. For all frequencies except 21.25 GHz both vertical and horizontal polarization is measured. At 21.25 GHz only vertical polarization (v-pol) is measured. This gives nine channels. The cone angle for the antenna look direction is approximately 49° relative to the spacecraft nadir. The scanning azimuth angle is about ±65° relative to the spacecraft x axis. The spacecraft operates in two yaw modes. For the yaw = 0° (180°) mode, the spacecraft x axis points in the direction (opposite direction) of the spacecraft velocity vector. Spacecraft yaw maneuvers are performed every 15–30 days, depending on season, to ensure a proper thermal environment for the spacecraft. The yaw maneuvers produce an abrupt change in the solar radiation impinging on TMI, and this complicates the calibration procedure.

The TRMM orbit is inclined 35° relative to the equator and as a result the swath of Earth observations is limited to 40°S–40°N. The inclined orbit was intended to provide dense coverage of the tropics. Another advantage of the inclined orbit is that it facilitates intersatellite comparisons. During every orbit the TMI swath crosses those of all other polar-orbiting MW sensors and, using a collocation window of 1 h, provides a huge number of satellite intercomparisons. In this paper, we used intercomparisons with the *F13* SSM/I, AMSR-E, and WindSat, which are three stable and well-calibrated sensors, to calibrate the TMI T_B. These intercomparisons, as well as those coming from other sensors not used for the calibration, show that TMI is a very stable sensor.

3. TMI PPS 1B11 data

The starting point for our TMI analyses and data processing is the most recent version of the TMI brightness temperatures orbital data files (1B11, version 7.002) produced by the Precipitation Processing System (PPS) at NASA GSFC (NASA 2011; Precipitation Processing System 2012). The T_B calibration for this PPS data is based on an RSS analysis of early TMI data from December 1997 through April 1998 (Wentz et al. 2001). The TMI calibration was adjusted to make the TMI T_B agree with the RSS version 4 (V4) of *F11*, *F13*, and *F14* SSM/I T_B. Later, an empirical time-varying T_B component was added to the 1B11 product to account for the varying temperature of the TMI antenna (Gopalan et al. 2009). This time-varying component has a zero mean and does not affect the overall absolute calibration based on the V4 SSM/I T_B. Our objectives here are 1) to update the V4 T_B calibration to the V7 calibration standard now used by all the other sensors and 2) to implement a more physical and exact method for dealing with the TMI antenna that is traceable back to the antenna's surface emissivity. This update also has the advantage of using 17 yr of TMI observations as compared to the 4 months used in the initial Wentz et al. (2000) analysis.

A first-step requirement for all RSS data processing is that the T_B coming from the satellite data provider (in this case PPS) be reversed back to the original sensor counts. Different data providers have different methodologies for converting radiometer counts to T_B. Also, the various data providers can implement their own version changes to the counts-to-T_B process, and these version changes are not always transparent to the users. By starting our analysis and data processing with the raw sensor counts, it is easier for us to maintain consistency, and we do not need to be concerned with the algorithm choices and changes of the data providers. For TMI, the counts-to-T_B algorithm used by GSFC was supplied by RSS back in 1999. This algorithm is easily inverted to yield raw sensor counts.

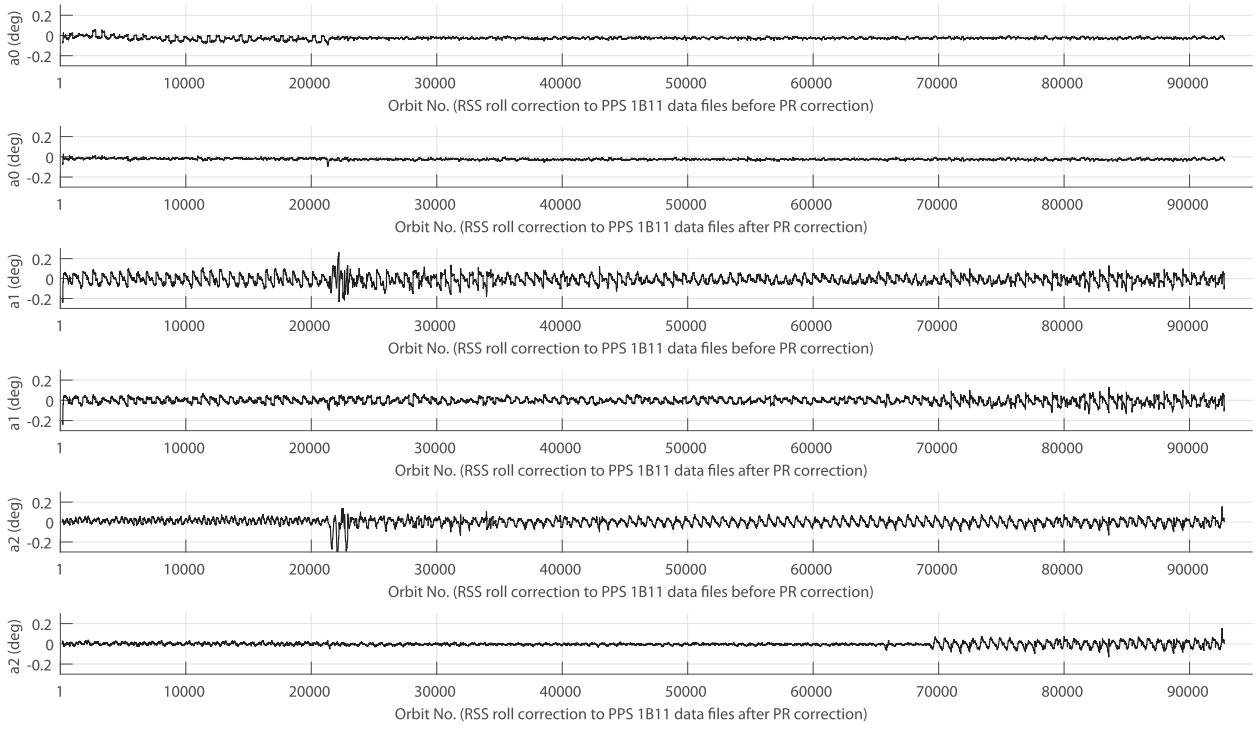

FIG. 1. The roll-correction coefficients a_0, a_1, and a_2 plotted for each orbit. Two cases are shown: before and after PPS implemented its PR-derived roll correction. Note that PPS roll correction stops at orbit 69 280.

Another component of the RSS processing is consistent geolocation. Rather than using the latitudes, longitudes, incidence angles, and such coming from the data provider, we use our own geolocation algorithm. The same tried-and-proven algorithm is used for all MW imagers. It is not uncommon to find errors in geolocation information provided by others. For the PPS TMI data, we find relatively large geolocation errors that are due to errors in the prelaunch sensor pointing angles.

4. Spacecraft roll error

Prior to version 7.002, the PPS 1B11 data had an error in specifying the spacecraft roll ϕ. This error revealed itself as a cross-track error in our SST retrievals. The roll error $\Delta\phi$ repeats every orbit with a slow time dependence on a time scale of days to weeks and is modeled as

$$\Delta\phi = a_0 + a_1 \sin\omega + a_2 \cos\omega, \qquad (1)$$

where ω is the orbit position angle going from 0° to 360° as the satellite goes through its orbit, starting at the southernmost point. The a coefficients are determined by a least squares fit based on the difference of the TMI SST retrieval $T_{S,\mathrm{TMI}}$ and a reference SST given by the NOAA SST operational product $T_{S,\mathrm{REY}}$ (Reynolds et al. 2002). The SST retrieval error resulting from the roll error is modeled as

$$(\Delta T_{S,\mathrm{TMI}})_\alpha = \frac{\partial T_S}{\partial \theta_i}\left(\frac{\partial \theta_i}{\partial \phi}\right)_\alpha \Delta\phi, \qquad (2)$$

where the first partial derivative is the error in the SST retrieval resulting from an error in specifying the Earth incidence angle θ_i and the second partial derivative is the change in θ_i produced by a change in roll. This second term is a function of the TMI scan position α. When TMI is looking forward ($\alpha = 0$), the roll error has little effect on θ_i. The maximum effect is when TMI is looking to the side. The a coefficients in (1) are found so as to minimize, in a least squares sense, the difference of the SST retrieval error given by (2) and the observed $T_{S,\mathrm{TMI}} - T_{S,\mathrm{REY}}$ difference. This fit is done for every TMI orbit using a moving ±15 orbit-averaging (±1 day) window. In this way, a table of a coefficients is found for every orbit.

The version 7.002 PPS 1B11 data files now have a roll correction applied, but only up to orbit 69 280. This roll correction is derived from the TRMM Precipitation Radar (PR) (Bilanow and Slojkowski 2006). The PR-derived roll correction is completely independent of our SST method. Figure 1 shows a_0, a_1, and a_2 derived from

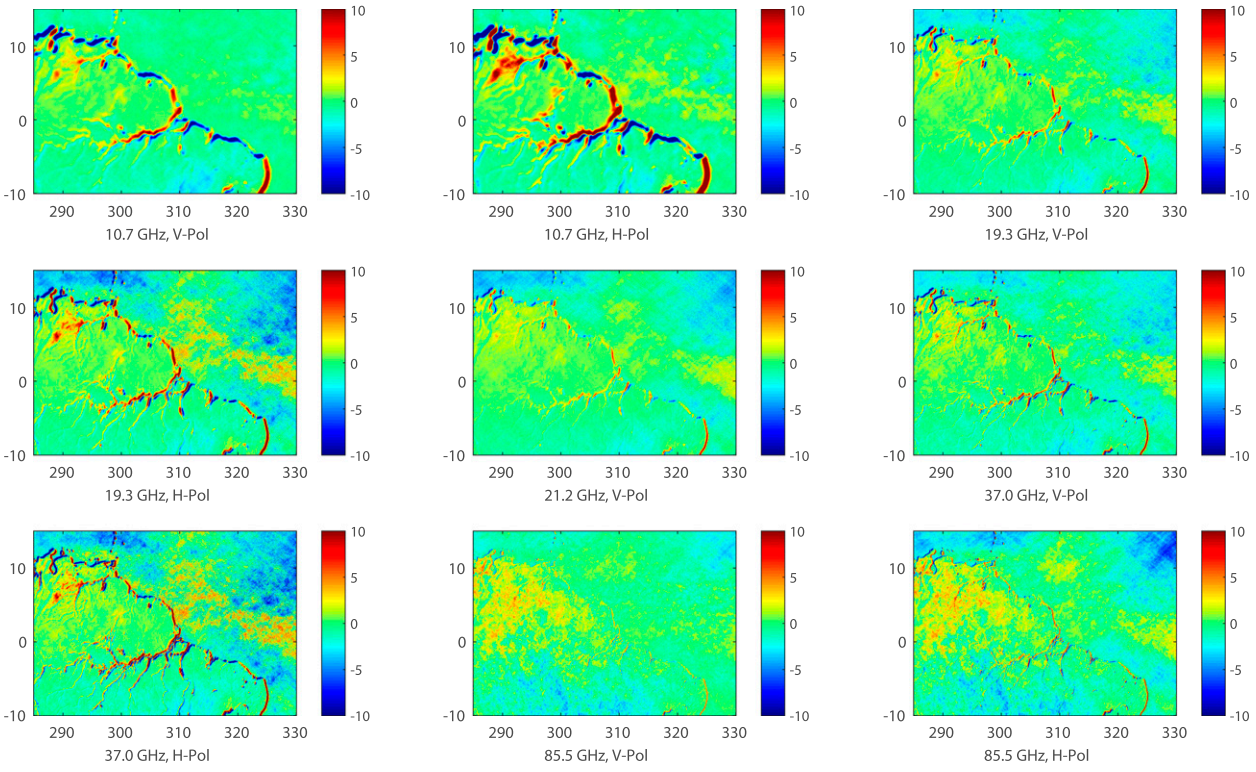

FIG. 2. Yaw 180° minus yaw 0° T_A imagery (K) of the Amazon basin. Red and blue halos indicate the imagery is misregistered.

the SST analysis plotted versus orbit number. Two sets of results are shown: one using PPS 1B11 data files without the PR roll correction and the other with the PR roll correction. The fact that the PR correction substantially reduces the size of a_2 and to a lesser extent a_1 indicates that the PR-derived and SST-derived roll corrections are consistent with each other. But note the abrupt increase in a_2 after orbit 69 280 at which point the PR correction is no longer done. Also note the large roll errors that occurred right after TRMM's orbit was boosted from 355 to 408 km near orbit 21 520. This was due to an attitude control problem, and both the SST-derived and PR-derived methods effectively correct this problem. For our analysis we use the SST-derived roll correction because it is available for the entire TMI mission.

5. Sensor pointing adjustment

After the spacecraft roll correction is applied, we evaluate the registration of the TMI antenna temperature T_A imagery relative to coastlines, islands, lakes, and rivers. Errors in the TMI imagery are most obvious when one looks at the difference between observations taken when the spacecraft is at yaw = 0° and when it is at yaw = 180°. A pointing error in the spacecraft along-track direction will shift the yaw = 0° imagery one way and the yaw = 180° the other. Figure 2 shows an example of this. The difference of the 180° minus 0° yaw T_A imagery of the Amazon basin for all nine TMI channels is shown. There is clearly a misregistration of the T_A imagery as evidenced by the blue and red halos. We have done this type of analysis for many other MW imagers, and the misregistration error of TMI is larger than typical, being about 10 km at 11 GHz.

The panels in Fig. 2 are for orbits 80 001–85 000. We spent considerable time looking at many other time periods and other locations and concluded that the misregistration is constant in time and can be mostly corrected by simply adjusting the TMI nadir cone angle θ_n and azimuth angle α_0 relative to the spacecraft x axis at the start of the scan. Table 2 gives the values of θ_n and α_0 used for the PPS 1B11 processing and the new values that we derive. Figure 3 shows the improved registration resulting from using the revised θ_n and α_0. There is obviously a big improvement in the registration but some small residual features remain. It is not clear if these features are lingering misregistration errors or if they are real differences resulting from the measurements from the two yaws being at different times. Since this set of figures only show the difference between the two yaws, we also present Fig. 4, which shows the T_A

TABLE 2. Revised TMI pointing angles.

Channels	GSFC 1B11 θ_n	Revised θ_n	GSFC 1B11 α_0	Revised α_0
11 GHz	49.00°	49.43°	64.402°	63.702°
19–85 GHz	49.00°	49.30°	64.402°	64.102°

imagery of the Hawaiian Islands just for yaw = 180°. The true location of the islands is shown in dark blue. A visual inspection of Fig. 4 suggests good absolute geolocation is now being achieved with the revised θ_n and α_0. We estimate the geolocation error is now about 1–2 km.

6. RFI in the cold mirror

The TMI cold mirror is designed to look upward into deep space, which has a known brightness temperature of 2.7 K. This cold-space observation along with the observation of the blackbody hot load provides two calibration references for converting the radiometer counts to antenna temperatures. Unfortunately, sometimes the cold mirror observes the transmission from geostationary communication satellites orbiting above TMI. This is a common problem for MW imagers. The time period over which this type of interference occurs is relatively short: several minutes during an affected orbit. The calibration of the MW radiometers tend to be fairly stable over these short time intervals, and the problem of RFI in the cold mirror is solved by discarding the period of erroneous cold counts and bridging the resulting time gap via interpolation.

Since the offending geostationary satellites are at fixed positions, the interference problem occurs at specific geographical locations. Geographic maps of the TMI cold counts are made to identify these locations. Figure 5 shows the TMI cold counts plotted versus the spacecraft nadir latitude and longitude. Each panel in the figure represents an average over 1000 orbits for which the zonal mean value has been subtracted, thereby giving maps of the cold-count anomaly. These anomaly maps show cold-mirror RFI only occurs for yaw = 0°. Also, the cold-mirror interference only occurs for the descending segment of the orbit except for one case that occurs at the northernmost extent of TRMM's orbit as the satellite is transitioning from ascending to descending. Table 3 gives the six types of cold-mirror RFI we identified by looking at the cold count anomaly maps. Figure 5 shows the anomaly maps corresponding to these six types. The RFI problem becomes greater in the latter part of the TMI mission. Bit masks are made of the anomaly areas shown in Fig. 5 and the cold counts in

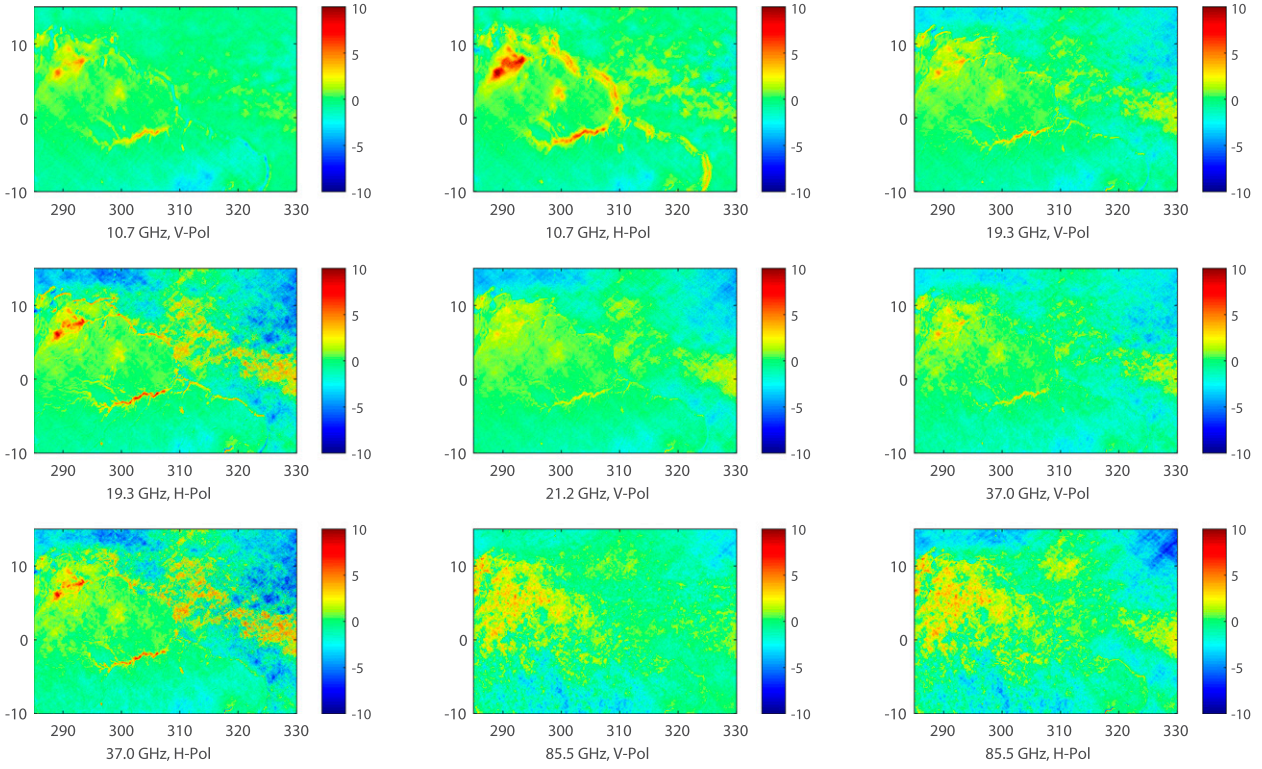

FIG. 3. As in Fig. 2, except that TMI pointing angles have been adjusted, resulting in better geolocation.

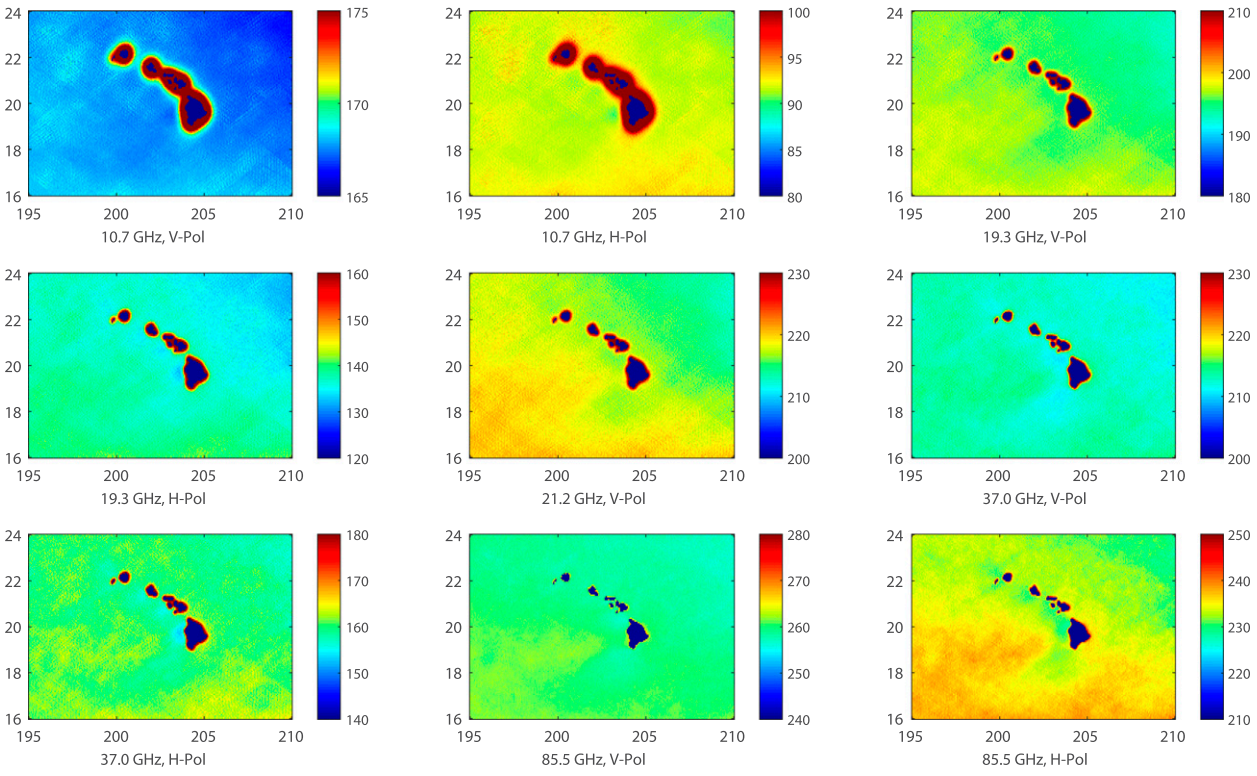

FIG. 4. Yaw 180° T_A imagery (K) of the Hawaiian Islands using revised TMI pointing angles. Correct locations are shown by the dark blue centers. Revised geolocation appears to be accurate.

these areas and time periods are flagged as bad. To fill in gaps thus created, a linear interpolation of cold counts versus time is done using the good cold counts on either side of the gap.

7. Antenna temperature calibration equation for an emissive antenna

By definition, the antenna temperature is a measure of radiant power entering the feedhorn. It is the brightness temperature of the surrounding environment integrated over the gain pattern of the TMI parabolic antenna and feedhorn assembly. It is common practice to segment this integration into a component coming from Earth and another coming from cold space:

$$T_{\mathrm{A0}} = (1-\eta)T_{\mathrm{Aert}} + \eta T_{\mathrm{Bspc}}, \tag{3}$$

where η is the fraction of power coming from cold space having a brightness temperature T_{Bspc} of 2.7 K and is called the spillover coefficient; T_{Aert} is the component of radiation coming from Earth. The subscript A0 denotes this expression applies to a perfectly reflecting antenna (emissivity is 0). MW antennas tend to mix polarizations and the term T_{Aert} represents a combination of vertical and horizontal polarization. For example, the v-pol port of the feedhorn will primarily consist of v-pol Earth radiation but there will also be a small horizontal-polarization (h-pol) component. Thus T_{Aert} is specified as

$$T_{\mathrm{Aert}} = \frac{1}{1+\chi}T_{\mathrm{Bco}} + \frac{\chi}{1+\chi}T_{\mathrm{Bx}}, \tag{4}$$

where χ is the cross-polarization coupling coefficient, T_{Bco} is the copolarization brightness temperature, and T_{Bx} is the cross-polarization T_B. For TMI we use the prelaunch antenna measurements to specify χ (given in Table 6).

For an emissive antenna like TMI some of the radiation comes from the antenna itself, and the radiation entering the feedhorn is

$$T_A = \varepsilon T_{\mathrm{ant}} + (1-\varepsilon)[(1-\eta)T_{\mathrm{Aert}} + \eta T_{\mathrm{Bspc}}], \tag{5}$$

where ε is the emissivity of the antenna and T_{ant} is the physical temperature of the antenna. Combining (3) and (5) gives

$$T_{\mathrm{A0}} = \frac{T_A - \varepsilon T_{\mathrm{ant}}}{1-\varepsilon}, \tag{6}$$

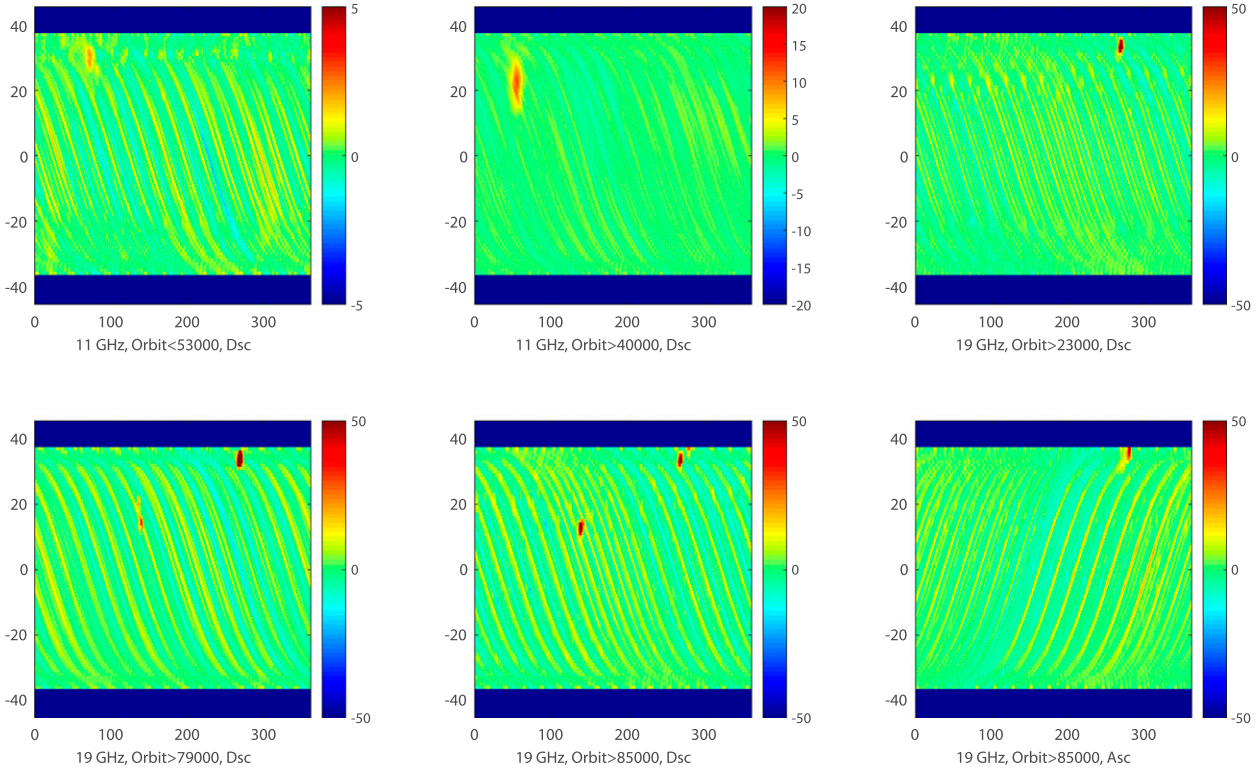

FIG. 5. Cold count anomaly maps that show the six types of cold-mirror RFI listed in Table 3. The red spots show areas where broadcasts from geostationary satellites are entering the TMI cold mirror. The orbital stripes are simply due to gain changes in the TMI channels and do not indicate RFI.

which provides the means to remove the emissivity effect. We note that (5) implicitly assumes all the cold-space radiation enters the feedhorn via the sidelobes of the antenna. In fact, some of the radiation may enter the feedhorn directly depending on the taper of the feedhorn pattern, and as such is not affected by ε. This is a subtle difference and amounts to about a 0.1-K difference in the modeling.

If the radiometer output has a linear response to T_A, then the antenna temperature is given by

$$T_{\text{Alin}} = \frac{(T_h - T_c)C_e + T_c C_h - T_h C_c}{C_h - C_c}, \tag{7}$$

where C_c, C_h, and C_e are the radiometer counts when the radiometer is looking at the cold mirror, the hot load, and Earth scene, respectively. The temperatures T_c and T_h are the effective temperatures of the cold and hot calibration targets. Equation (7) is simply expressing the assumption that the radiometer counts vary linearly as the scene temperature varies from T_c to T_h. To account for nonlinearity in the radiometer's response function, the usual method is to introduce the following quadratic term when estimating T_A:

$$T_A = T_{\text{Alin}} - \beta(T_A - T_c)(T_h - T_A), \tag{8}$$

where β is a measure of the nonlinearity. The quadratic term accounts for the fact that the nonlinearity has no effect when the incoming radiation is at the same temperature as either the hot-load temperature T_h or cold-load temperature T_c. Solving the quadratic equation gives

$$T_A = \frac{1 + \beta(T_c + T_h) - \sqrt{[1 + \beta(T_c + T_h)]^2 - 4\beta(T_{\text{Alin}} + \beta T_c T_h)}}{2\beta}. \tag{9}$$

Equations (6), (7), and (9) provide the means to compute the antenna temperature T_{A0}, free of emissivity effects, given the radiometer counts, the cold- and hot-load temperatures, T_c and T_h, the antenna emissivity

TABLE 3. Types of cold-mirror RFI (only affects yaw = 0°).

Orbits affected	Frequency	Orbit direction
<53 000	11 GHz	Descending
>40 000	11 GHz	Descending
>23 000	19 GHz	Descending
>79 000	19 GHz	Descending
>85 000	19 GHz	Descending
>85 000	19 GHz	Ascending

ε and temperature T_{ant}, and the nonlinearity coefficient β. As a starting point, we use the emissivity values reported by Wentz et al. (2001) and assume a linear radiometer ($\beta = 0$). These values are later revised as discussed below. The remaining term that needs specifying is the physical temperature of the antenna T_{ant}.

8. Physical temperature of the antenna

There are no thermistors attached to the TMI antenna and hence other means are required to estimate its physical temperature T_{ant}, which we express as

$$T_{\text{ant}} = \overline{T}_{\text{ant}} + \Delta T_{\text{ant}}, \tag{10}$$

where $\overline{T}_{\text{ant}}$ is the mission-average reflector temperature and ΔT_{ant} is its variation. Because of other possible sources of biases in the T_A calibration equation, it is difficult to uniquely specify $\overline{T}_{\text{ant}}$. Previous results (Wentz et al. 2001) suggest a value near 290 K. During the course of this analysis, we experimented with two values: 280 and 290 K. The value for ε is between 0.025 and 0.050, and a 10-K change in $\overline{T}_{\text{ant}}$ represents a change from 0.25 to 0.50 K in the absolute bias of T_A. The nature of the calibration process is such that any change in $\overline{T}_{\text{ant}}$ results in a compensating change in the spillover η (see next section). We found that using a value of $\overline{T}_{\text{ant}} = 280$ K, as compared to 290 K, results in spillover values closer to prelaunch values. A colder value seems unreasonable in view of the Wentz et al. (2001) results, so 280 K is our choice for $\overline{T}_{\text{ant}}$. The more important and difficult problem is specifying the variation in T_{ant} over the mission life of TMI.

Our first approach to estimating ΔT_{ant} was to use a retrieval algorithm similar to the ones we use for geophysical retrievals (Wentz and Meissner 2007). Variations in T_{ant} produce distinctive variations T_A that have a specific spectral and polarimetric signature as dictated by (5). A simple linear retrieval algorithm is derived in the same manner that we derive the geophysical retrieval algorithm. A set of simulated antenna temperatures for a large ensemble of ocean scenes is generated using the RTM along with (5) to simulate the emissive antenna. For each scene, T_{ant} is varied by ±50 K about its mean value. Using these scenes, an algorithm of the following form is trained in a least squares sense to estimate the variation ΔT_{ant}:

$$\Delta\hat{T}_{\text{ant}} = \sum_{i=1}^{7} p_i [f(T_{Ai}) - f(\overline{T}_{Ai})], \tag{11}$$

where subscript i denotes the seven lower TMI channels (from 11V to 37H), T_{Ai} is the TMI measurement, and $\overline{T}_{Ai}$ is the antenna temperature for $T_{\text{ant}} = \overline{T}_{\text{ant}}$. For all channels other than the 21-GHz v-pol channel (21V), the function f is defined as $f(x) = x - 150$ and for 21V, $f(x) = -\ln(290 - x)$, which is a common method for removing the nonlinearity effects that occur near the 22.235-GHz water vapor line (Wentz and Meissner 2007). The algorithm's p coefficients have a slight dependence on the Earth incidence angle θ_i, and Table 4 gives their values for $\theta_i = 53.3°$.

Equation (11) is used to estimate T_{ant} for every TMI ocean observation. The estimation error for a single observation is quite noisy, but by averaging over one day (15 orbits), the noise is substantially reduced. When doing the averaging we assume that, for a given local time and yaw (i.e., solar environment) within the orbit, ΔT_{ant} is nearly the same over the course of a day. Thus the averaging is stratified into 0.5-h local time bins. To specify $\overline{T}_{Ai}$, we use the daily mean T_{Ai} averaged over all local times.

We experimented with using $\Delta\hat{T}_{\text{ant}}$ to remove the emissive antenna effects. A good indicator of the algorithm's performance is the veracity of the SST retrieval because this retrieval is quite sensitive to error in specifying ΔT_{ant}. When the SST retrievals were compared to the Reynolds SST, there were significant differences that were correlated with the local time (i.e., solar environment) of the TMI observations. It was clear that these differences were not due to true diurnal effects. Rather, they were as a result of deficiencies the $\Delta\hat{T}_{\text{ant}}$ estimate, which is just based on the T_A observation. We decided to supplement the estimate of ΔT_{ant} with additional temperature information provided by the TMI thermistors. Although these

TABLE 4. Coefficients for the ΔT_{ant} retrieval algorithm ($\theta_i = 53.3°$).

p_1	p_2	p_3	p_4	p_5	p_6	p_7
−3.910 77	11.996 39	−6.734 30	1.163 49	75.399 28	18.575 07	−10.083 91

TABLE 5. Coefficients for the ΔT_{ant} blended algorithm.

Yaw	c_0	c_1	c_2	c_3	c_4	c_5	c_6	c_7	c_8	c_9	c_{10}	c_{11}
0°	−1.334 29	0.077 17	−0.064 50	−0.173 73	−0.079 84	0.009 48	−0.058 25	−0.070 42	0.001 10	−0.015 52	0.006 36	0.008 55
180°	−1.002 87	0.062 07	−0.051 64	−0.164 07	−0.150 69	−0.124 50	−0.059 95	−0.057 97	0.002 82	−0.034 53	0.005 21	0.006 06

thermistors are not attached to the antenna, they can be used as proxies of the thermal environment. There are three thermistors attached to the external hot load, one to the external top surface of the TMI drum enclosure, and one other attached to the 85-GHz receiver shelf. Let t_1 (degree Celsius) denote the average of the three hot-load thermistors, and let t_2 and t_3 (degree Celsius) denote the drum temperature and the mixer temperature. Let $\overline{t_1}$, $\overline{t_2}$, and $\overline{t_3}$ denote their average over a single orbit. These orbit-averaged values have the property that they slowly vary in time, having nearly the same value from one orbit to the next. As such, they provide information on the slowly varying component of ΔT_{ant} as the solar environment changes over days to weeks. Proxies for the rapidly changing part of ΔT_{ant} that occurs within each orbit are given by the change in thermistor readings relative to their orbital average, as is denoted by $\delta_i = t_i - \overline{t_1}$. This thermistor information is blended with the $\Delta\hat{T}_{\text{ant}}$ estimate from (11) by doing the following least squares fit to the TMI minus Reynolds SST differences (very similar to how roll errors were found in section 4):

$$T_{S,\text{TMI}} - T_{S,\text{REY}} = c_0 + \left(\sum_{i=1}^{3} c_i\overline{t_i} + c_{i+3}\delta_i\right) + c_7\Delta\hat{T}_{\text{ant}} + c_8\delta_3\overline{t_1} + c_9\delta_3\delta_2 + c_{10}\delta_3^2 + c_{11}\Delta\hat{T}_{\text{ant}}\delta_2. \quad (12)$$

This fit is done using TMI orbits 144–14 200, which is about 2.5 yr of data, thereby finding c_0 through c_{11}. The form for (12) that best represented the SST difference was determined by trial and error. A separate set of c coefficients is found for yaw = 0° and 180° and given in Table 5. The variation in the temperature of the antenna about its mean value is then given by

$$\Delta T_{\text{ant}} = \left(\frac{\partial T_S}{\partial T_{\text{ant}}}\right)^{-1}\Lambda, \quad (13)$$

where Λ denotes the right-hand side of (12) and the sensitivity of T_S to T_{ant} is modeled as a constant value of −0.0617. Figure 6 shows ΔT_{ant} plotted versus local time and day of year for the entire TMI mission up to early 2014. The antenna reaches its maximum temperature for local time near 1900 for which ΔT_{ant} has a value near 25 K. The minimum value of about −25 K occurs near 0500 LT. The dependence of ΔT_{ant} on yaw is obvious from the vertical striping in Fig. 6.

9. Amazon forest calibration

When calibrating the set of 11 MW imagers listed in Table 1, our usual approach is to calibrate to the ocean RTM and then verify the calibration over land targets. For the most part, the radiometers are sufficiently linear that no further calibration is needed over land. For TMI, the calibration problem becomes more complex because of the emissive antenna. To simplify the problem and separate the estimation of the various calibration parameters, we use an area in the northern Amazon basin as a calibration reference in addition to the ocean. The antenna temperature of the Amazon forest is near 275 K, which is similar to the physical temperature of the antenna T_{ant}, and as a result the sensitivity of T_A to ε is very small, as is shown by its partial derivative derived from (5):

$$\frac{\partial T_A}{\partial \varepsilon} = T_{\text{ant}} - T_{\text{Aert}} + \eta(T_{\text{Aert}} - T_{\text{Bspc}}). \quad (14)$$

This property helps to separate the derivation of η from the derivation of ε. The emission from the Amazon forest is nearly unpolarized, and as a result T_{Aert} given by (4) equals T_{Bco} to within 0.02K. Inverting (3) to yield η and setting $T_{\text{Aert}} = T_{\text{Bco}}$ gives

$$\eta = \frac{T_{\text{Bco}} - T_{\text{A0}}}{T_{\text{Bco}} - T_{\text{Bspc}}}, \quad (15)$$

where T_{A0} is the TMI measurement, corrected for emissivity effects according to (6), and T_{Bco} is the ''true'' brightness temperature of the Amazon forest. To specify T_{Bco}, we use the region 1°S–3°N, 301°–308°E as our calibration target. This region has been used by other investigators (Brown and Ruf 2005; Meissner and Wentz 2010). It is heavily forested and has remained stable for the last couple of decades. We have a large database of Amazon T_B measurements collected from the all the MW imagers listed in Table 1. We only used observations from 0100 to 0500 local time to avoid

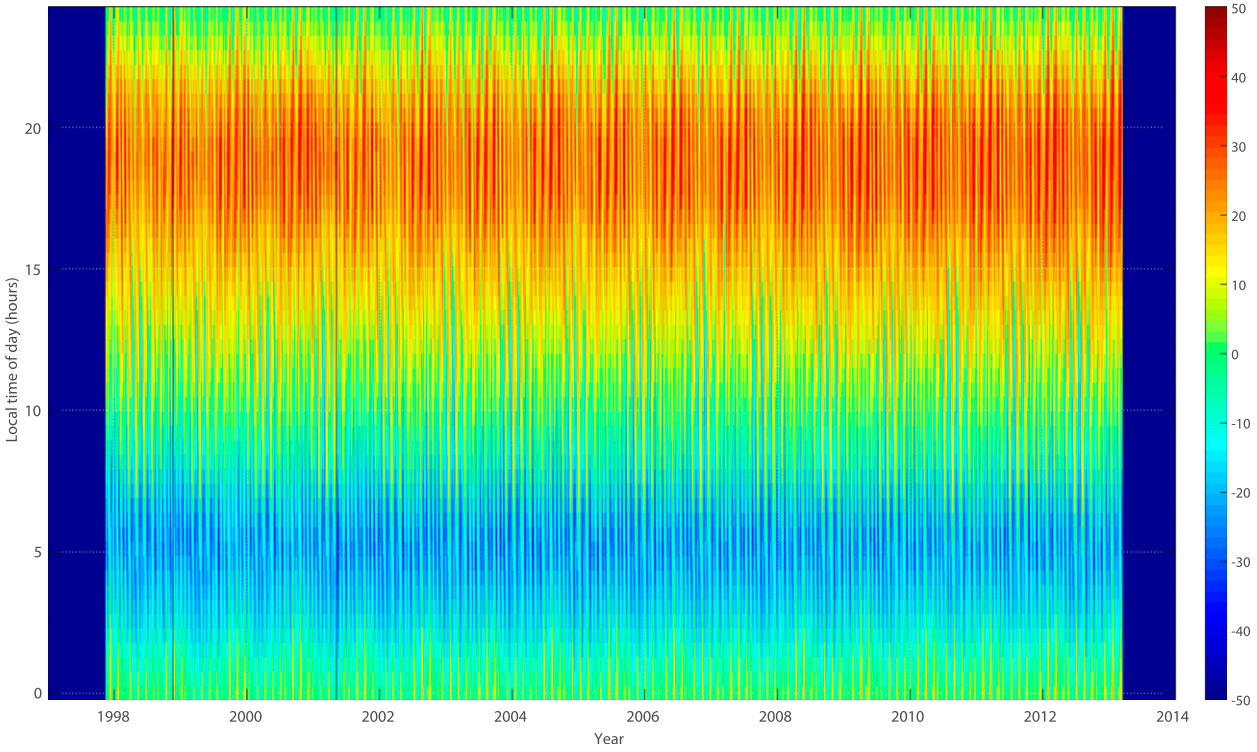

FIG. 6. Variation ΔT_{ant} of the temperature of TMI's antenna relative to a mean temperature of 280 K; ΔT_{ant} is found at 48 different local times (i.e., 30-min intervals) for each day.

diurnal warming problems, and a diurnal model (Mo 2007) is used to normalize all observations to 0130 LT. We average the results from all sensors to obtain a reference T_B value for the TMI calibration. Table 6 gives this sensor-averaged T_B value and the standard deviation of the T_B values for the individual sensors. These sensor-averaged values are used to specify T_{Bco}, and (15) is used to compute postlaunch spillover values. The prelaunch and Amazon-derived values of η are given in Table 6. Values are given for each of the nine TMI channels. In some cases, the frequencies of the reference sensors are not quite the same as the TMI channels, but these differences are small and are not a real issue.

10. Ocean calibration

To find the other terms in the T_A calibration equation, we use the ocean as a calibration reference. The Meissner and Wentz (2012) ocean RTM is used to generate a simulated T_A. The RTM requires the specification of SST, wind speed W, and direction φ, as well as columnar water vapor V and cloud liquid water L. We only use observations that are free of rain as determined by the TMI rain algorithm. For the frequencies we are considering, the atmospheric component of T_A is primarily a function of the columnar amount of vapor and liquid water rather than the detailed shape of the vertical profiles (Wentz 1997). Furthermore, SST and V serve as proxies for the air temperature profile. Variations in the profile shape and temperature from typical values will produce errors in the RTM, but these errors are small and by design have a zero mean.

Recently, the accuracy of the RTM was tested by comparing its predicted T_B with the measurements from the Global Precipitation Measurement (GPM) Microwave Imager (GMI) launched in February 2014. The RTM predates GMI, and hence GMI provides an independent assessment of the RTM. Much effort was put into GMI's prelaunch calibration because GMI is to serve as a calibration standard for current and future MW imagers. For all channels from 11 to 89 GHz, the difference between the GMI measured T_B and the RTM was always less than 0.8 K (Draper et al. 2015). Considering that the GMI absolute accuracy requirement is 1.3 K, these GMI minus RTM differences may be mostly due to small calibration errors with GMI rather than the RTM.

The inputs to the ocean RTM are as follows. SST comes from the Reynolds optimum interpolation (OI)

TABLE 6. Amazon forest reference brightness temperature and antenna spillover and cross polarization.

Channel	Mean T_B (K)	Std dev T_B (K)	η_0 (prelaunch)	η (Amazon)	$280(\eta-\eta_0)$ (K)	χ (prelaunch)
11V	281.72	0.08	0.016 00	0.019 60	1.01	0.003 67
11H	280.33	0.11	0.016 00	0.019 30	0.92	0.004 59
19V	282.33	0.51	0.021 80	0.025 45	1.02	0.004 31
19H	281.57	0.43	0.022 50	0.024 66	0.60	0.004 52
21V	281.62	0.31	0.024 30	0.022 13	−0.61	0.005 77
37V	281.01	0.38	0.012 50	0.018 39	1.65	0.023 85
37H	280.43	0.32	0.012 30	0.017 31	1.40	0.018 56
85V	282.30	0.33	0.012 10	0.017 73	1.58	0.020 03
85H	282.18	0.51	0.010 80	0.021 06	2.87	0.029 34

product (Reynolds et al. 2002, 2007a,b) interpolated to the location of the TMI footprint. For W, V, and L we use the geophysical retrievals from the *F13*, AMSR-E, and WindSat. These three sensors cover the entire mission life of TMI. We require the retrievals be within 1 h and 25 km from the TMI observation. For wind direction, we use the National Centers for Environmental Prediction Global Data Assimilation System 6-hourly wind fields (NCEP 2000). A large database of TMI and RTM T_A pairs ($T_{A,\mathrm{TMI}}$, $T_{A,\mathrm{RTM}}$) is thus constructed and analyzed in several different ways.

We first determine the nonlinearity coefficients β and find optimum values of the antenna emissivities ε now that the antenna physical temperature has been specified. Values for β and ε are found so as to minimize the least squares variance of $T_{A,\mathrm{TMI}} - T_{A,\mathrm{RTM}}$, and these values are shown in Table 7. Also shown is the change in the ocean T_A that occurs when β is applied. The Wentz et al. (2001) values of ε ranged from 0.027 to 0.040 and showed no obvious spectral dependence. In comparison, the rederived emissivity values range from 0.025 to 0.049 with a clear spectral dependence of increasing with frequency. This tendency for the emissivity to increase with frequency is similar to that observed for the *F16* SSM/IS, which also has an emissive antenna (Kunkee et al. 2008).

Another possible source of error for MW imagers is mispecification of the effective hot-load temperature T_h. The temperature of the TMI hot load is measured by three thermistors, which are averaged together to obtain T_h. However, thermal gradients in the load will cause the effective temperature of the load, as seen by the feedhorn, to be different from the thermistor readings. To assess this potential problem, we stratify the $T_{A,\mathrm{TMI}} - T_{A,\mathrm{RTM}}$ difference according to the sun's azimuth angle φ_{sun} and zenith angle θ_{sun} as measured in the spacecraft coordinate system for which the z axis points up away from nadir and the x axis is the spacecraft velocity vector. These (φ_{sun}, θ_{sun}) binned values are averaged over the TMI mission. The T_A difference is converted to an error ΔT_h in specifying the hot-load temperature using

$$\Delta T_h = -\frac{T_h - T_c}{T_A - T_c}(T_{A,\mathrm{TMI}} - T_{A,\mathrm{RTM}}). \qquad (16)$$

This expression comes from the T_A calibration equations and expresses the fact that the error in T_A resulting from an error in T_h decreases linearly to zero as T_A goes from T_h to T_c. The leading minus sign is applied because ΔT_h is added to the thermistor-inferred T_h. Figure 7 shows ΔT_h plotted versus the sun angles φ_{sun} and θ_{sun} for the nine TMI channels. There is a good deal of interchannel consistency in the ΔT_h plots. The small interchannel differences in ΔT_h could be due to any number of small residual errors in the analysis. Or, the

TABLE 7. Antenna emissivity, nonlinearity coefficient, and preboost bias.

Channel	ε	β (K^{-1})	β change to ocean T_A (K)	Preboost bias (K)
11V	0.032 18	0.857×10^{-5}	−0.16	−0.10
11H	0.024 95	0.382×10^{-4}	−0.63	−0.18
19V	0.036 01	-0.430×10^{-4}	0.69	−0.13
19H	0.036 82	-0.518×10^{-4}	0.98	−0.24
21V	0.036 88	-0.456×10^{-4}	0.60	−0.05
37V	0.037 93	-0.555×10^{-4}	0.78	−0.17
37H	0.038 18	-0.300×10^{-4}	0.56	−0.26
85V	0.048 58	-0.691×10^{-4}	0.36	−0.10
85H	0.048 52	-0.758×10^{-4}	0.81	−0.21

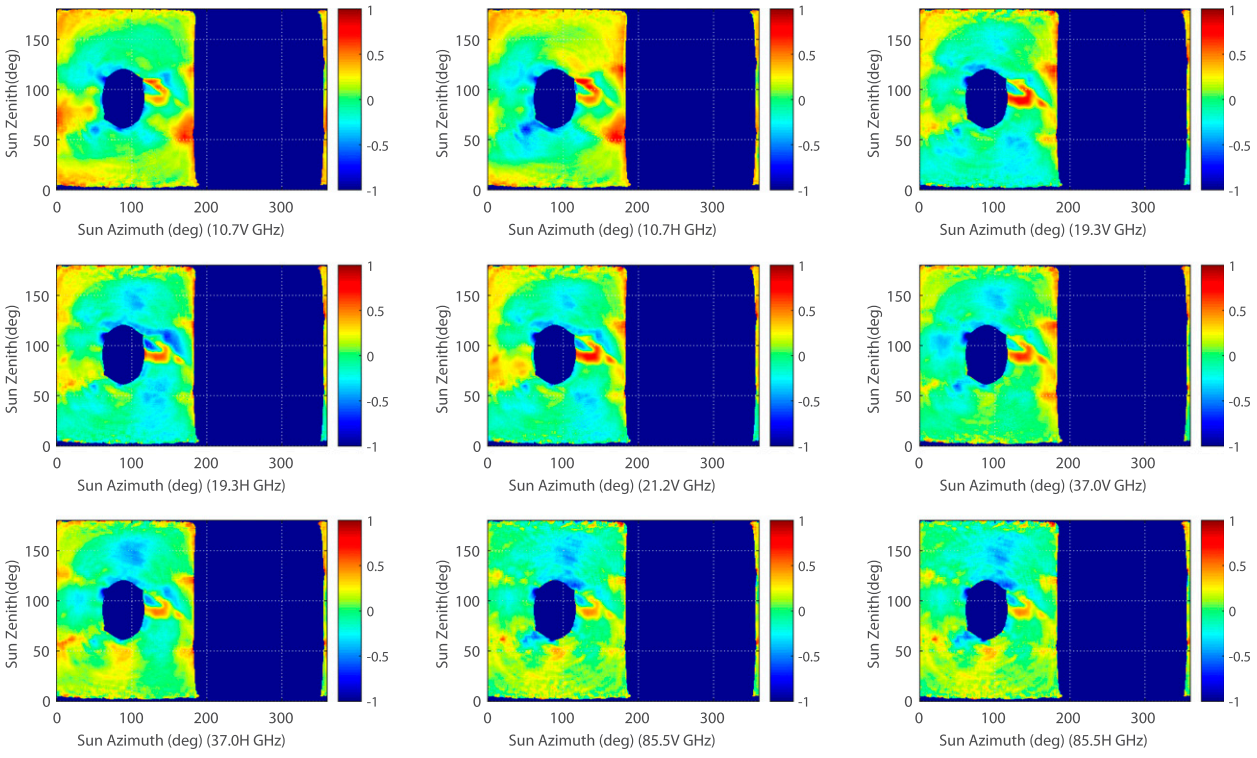

FIG. 7. Correction to the hot-load temperature (K) as a function of the sun azimuth and zenith angles. Dark blue areas are regions not sampled by TMI.

differences may be an indication of varying penetration depths and horizontal sampling of the load by the feedhorn. We found small but systematic differences in the $\Delta T_h(\varphi_{\text{sun}}, \theta_{\text{sun}})$ plots when stratified according to the two yaws and separate corrections are applied for each yaw. Figure 7 shows the results for yaw = 180°.

We also look at the effect of the TRMM's orbit being boosted from 355 to 408 km in August 2001. The *F13* observations bridge this change in the TRMM altitude and provide the means to evaluate the pre- versus postboost TMI T_A. The increase in altitude increases the Earth incidence angle θ_i, but this effect is accounted for when computing $T_{A,\text{RTM}}$. The $T_{A,\text{TMI}} - T_{A,\text{RTM}}$ difference was computed before the boost and 20 000 orbits after the boost. Small differences on the order of 0.1–0.2 K are found and are given in Table 7 for each channel. These small offsets are subtracted from the preboost T_A. It is not clear what causes these biases. They do not have the signature of an error related to θ_i. Possibly the difference in the pre- versus postboost thermal environment is not being modeled quite correctly.

Wentz et al. (2001) reported along-scan errors in the TMI observations related to the scan angle α and derived a correction based on both cold-space observations and ocean observations. We revisited this problem using the technique just described for finding ΔT_h. In this case, the $T_{A,\text{TMI}} - T_{A,\text{RTM}}$ differences are stratified according to α. The along-scan errors found by this new analysis, which uses 17 yr of TMI observations, are within 0.1 K of that found by Wentz et al. (2001). This demonstrates that the along-scan errors are very stable in time. For the V7 TMI calibration, we use the new values.

11. Analysis of calibrated antenna temperatures

All of the calibration adjustments discussed above are applied to the TMI observations, and calibrated T_A are found. Figure 8 shows the difference of the TMI-calibrated T_A minus the RTM T_A computed using *F13*, AMSR-E, or WindSat geophysical retrievals. The differences are plotted versus orbit number and orbit position angle ω, and this is called a mission plot because it is useful for looking at the entire mission of a given sensor. A moving window of ±300 orbits is used for averaging. Table 8 gives the mean and standard deviations of the T_A differences preaveraged over ±300 orbits in time and 3.6° in ω. By design, the mean $T_{A,\text{TMI}} - T_{A,\text{RTM}}$ is near zero (0.00–0.02 K). For the lower frequencies (11–37 GHz) the standard deviation

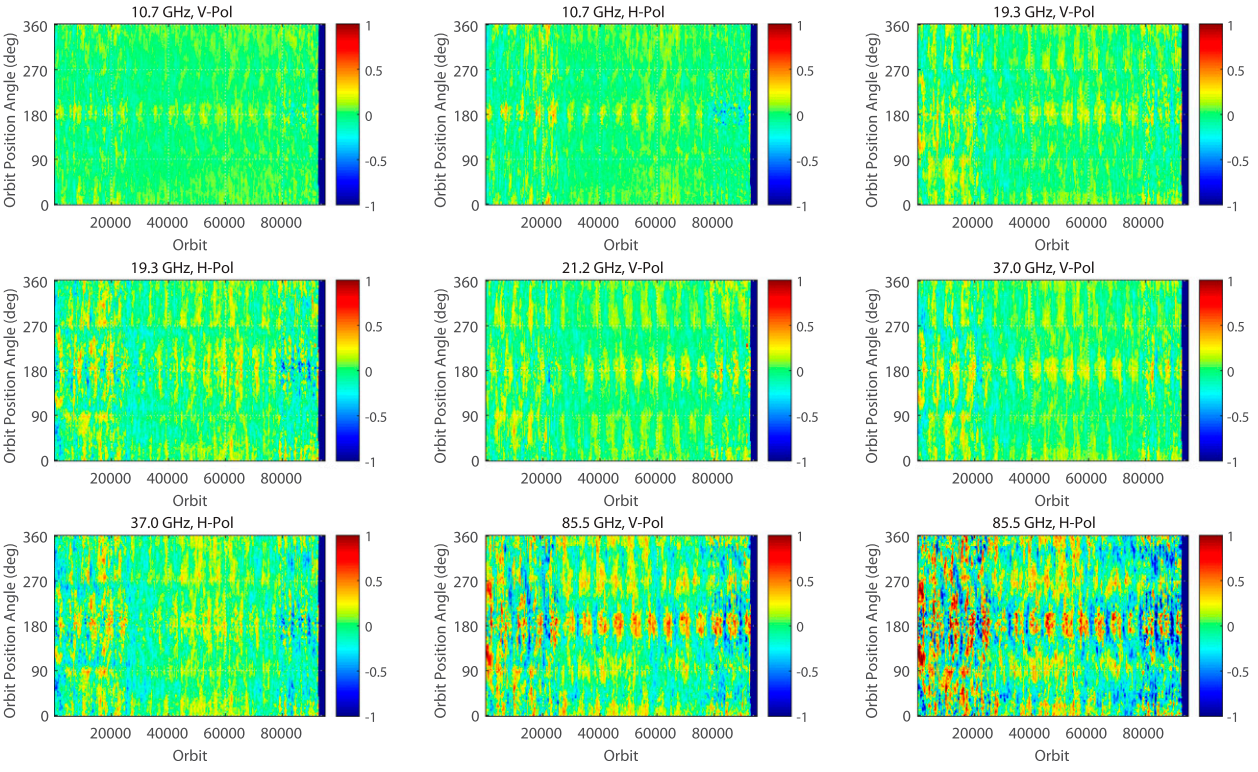

FIG. 8. TMI mission plot showing RSS-calibrated $T_{A,\mathrm{TMI}}$ minus $T_{A,\mathrm{RTM}}$ (K). Each panel corresponds to a different TMI channel. The y axis is the orbit position of TMI as it goes from 40°S to 40°N and back again to 40°S. The x axis is the orbit number. The $T_{A,\mathrm{RTM}}$ comes from a combination of three other microwave imagers: *F13*, AMSR-E, and WindSat.

of $T_{A,\mathrm{TMI}} - T_{A,\mathrm{RTM}}$ is between 0.07 and 0.18 K. The standard deviations are somewhat higher at 85 GHz, where the influence of clouds, which have high spatial/temporal variability, dominates the statistics. For some channels the geographic variation of T_A is about 50 K, and a standard deviation of 0.1 K represents a 0.2% modeling and calibration error. There is some slight vertical banding in Fig. 8 that is related to transitioning to and from the three calibration sensors. The *F13* overlap is from the beginning of the TMI mission to orbit 68 200. The AMSR-E overlap is for orbits 25 915–79 089, and the WindSat overlap is for orbit 29 793 to the end of the TMI mission.

For perspective, we also include the results we obtain when using the brightness temperature values in the PPS 1B11 data files. The 1B11 results are shown in Fig. 9 and Table 8. The 1B11 T_B show large biases (1–2 K) relative to the RTM. To stay within the ±1-K color bar, these large overall biases have been removed when making Fig. 9. Still there are relatively large residual features (±1 K) in the 1B11 mission plot, which manifest themselves as higher standard deviations in Table 8. The PPS

TABLE 8. TMI mission plot statistics for RSS and PPS calibration.

Channel	V7 mean (K) $T_{A,\mathrm{TMI}} - T_{A,\mathrm{RTM}}$	V7 std dev (K) $T_{A,\mathrm{TMI}} - T_{A,\mathrm{RTM}}$	1B11 mean (K) $T_{B,\mathrm{TMI}} - T_{B,\mathrm{RTM}}$	1B11 std dev (K) $T_{B,\mathrm{TMI}} - T_{B,\mathrm{RTM}}$
11V	0.000	0.068	−1.078	0.111
11H	−0.006	0.091	−1.735	0.141
19V	0.001	0.111	0.113	0.249
19H	−0.010	0.154	−1.102	0.316
21V	0.000	0.114	0.093	0.307
37V	−0.004	0.126	−2.461	0.176
37H	−0.021	0.178	−1.448	0.253
85V	−0.005	0.246	−1.591	0.254
85H	−0.020	0.341	−2.172	0.378

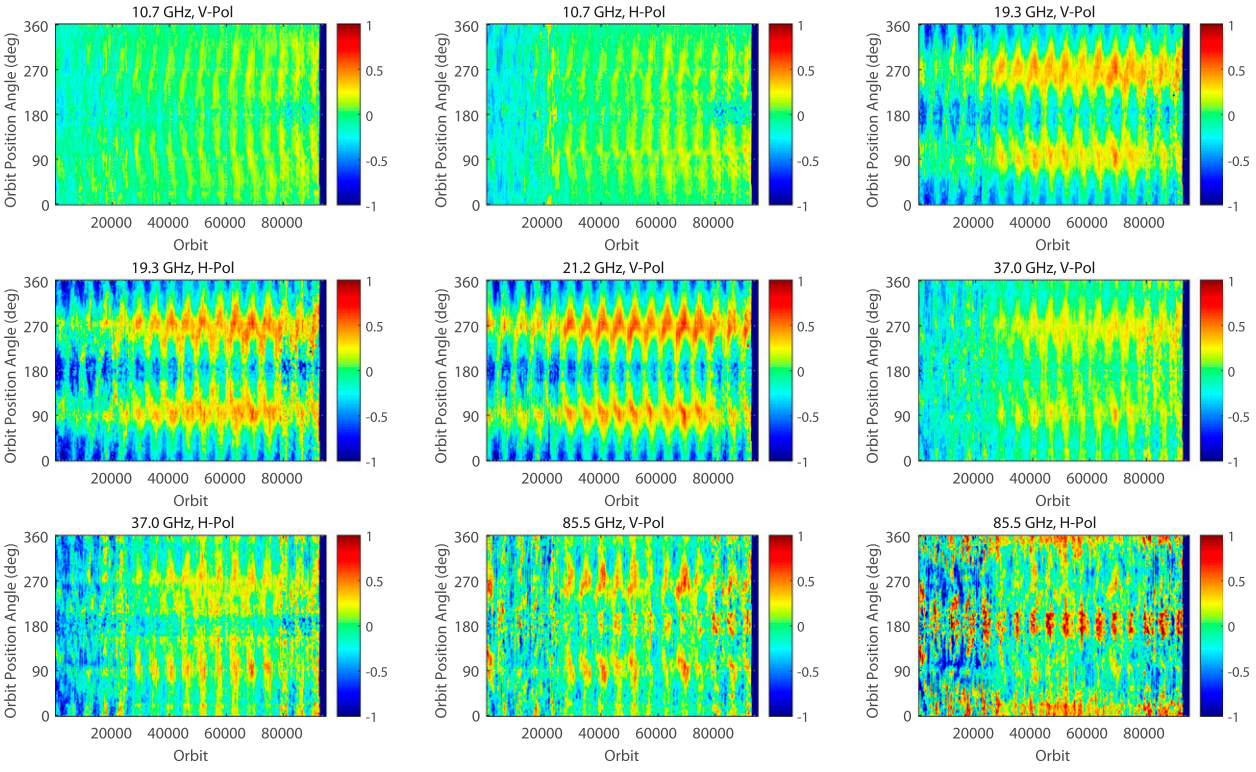

FIG. 9. As in Fig. 8, but the PPS-calibrated $T_{B,\mathrm{TMI}}$ is used instead of the RSS-calibrated $T_{B,\mathrm{TMI}}$. The large biases shown in Table 8 have been removed to keep the differences within the ±1-K color bar.

statistics are in terms of T_B rather than T_A, but the difference is negligible: $\Delta T_A \approx 0.98 \Delta T_B$.

12. Intersatellite comparisons of environmental parameters

In this section, we compare the TMI retrievals of SST, wind speed, water vapor, cloud liquid water, and rain rate (Wentz et al. 2015) with similar retrievals from other MW sensors. The differences of these environmental parameters (other MW sensor minus TMI) are denoted by ΔT_S, ΔW, ΔV, ΔL, and ΔR. A collocation window of ±1 h and ±25 km is used in the analyses. These comparisons are done globally over all ocean regions observed by TMI (40°S–40°N).

For all MW imagers, we use the same type of retrieval algorithm, and this helps to achieve consistency among the retrievals from different sensors. The retrieval algorithm is described by Wentz and Spencer (1998), Chelton and Wentz (2005), and Wentz and Meissner (2007). The rain retrieval part of the algorithm is further detailed in Wentz and Spencer (1998) and Hilburn and Wentz (2008a). The retrieval algorithm is designed to be, as much as possible, the inverse of the RTM. By inverse we mean the following:

$$\Gamma[\mathbf{T}_{\mathrm{Brtm}}(\mathbf{E}_p)] = \mathbf{E}_p, \tag{17}$$

where Γ represents the retrieval algorithm with the input being the set $\mathbf{T}_{\mathrm{Brtm}}$ of brightness temperatures computed from the ocean RTM assuming a set $\mathbf{E}_p$ of environmental parameters. The desired property is that the retrieved environmental parameters equal the ones used to compute $\mathbf{T}_{\mathrm{Brtm}}$. Equation (17) in effect defines the retrieval algorithm in terms of the RTM. This inverse property (17) helps to ensure that the T_B calibration results in a proper E_p calibration, as is shown in this section. It also greatly facilitates the overall calibration process by reducing the problem to a function of four variables (T_S, W, V, and L). The retrieval algorithm uses all TMI channels except for two 85-GHz channels. The rain rate retrieval uses a separate algorithm (Wentz and Spencer 1998), for which the W, V, and L retrievals serve as input.

Figures 10–14 show the time series of the monthly averages of ΔT_S, ΔW, ΔV, ΔL, and ΔR, respectively. For each time series, these figures show the mean values of ΔE_p, called offset, and the drift in ΔE_p. The drift is defined as the least squares slope of the time series times the duration of the time series and hence is a measure of the change in ΔE_p over the period of

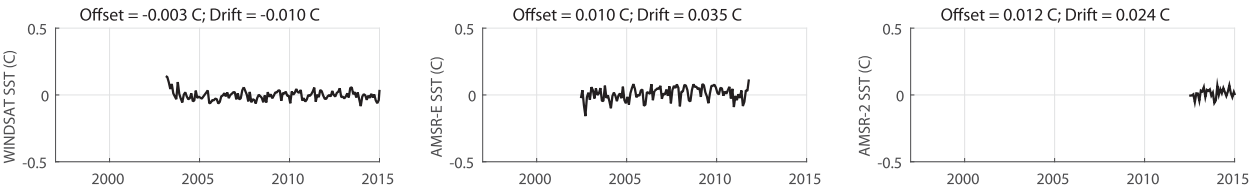

FIG. 10. Time series of monthly SST retrievals (°C) from three MW imagers compared to TMI.

overlap. For Fig. 10, which shows SST, there are only three other sensors that provide SST retrievals: WindSat, AMSR-E, and Advanced Microwave Scanning Radiometer 2 (AMSR-2). For the other figures, there are a total of nine MW imagers that can be compared to TMI. Furthermore for Fig. 11, which shows wind speed, there are two additional sensors: the scatterometers QuikScat and Advanced Scatterometer (ASCAT).

Given this many comparisons, certain problems with some of the MW imagers become obvious. These problems are listed in Table 9. The most notable problems are with the *F15* SSM/I and the *F16* SSM/IS. On 14 August 2006, a radar calibration beacon (RADCAL) was activated on the *F15* satellite. Although we have taken measures to correct this problem (Hilburn and Wentz 2008b; Hilburn 2009), the retrievals are still quite noisy during the RADCAL period, which is shown in red in Figs. 11–14. Also shown in red is the time period starting in 2009 for *F16*, during which the *F16* retrievals significantly degrade. The *F16* SSM/IS is our most problematic sensor. It has an emissive antenna, sun intrusion into the hot load, and an orbit with a rapidly drifting ascending node time. Clearly, we need to revisit our calibration of *F16*. Of minor note is that the last year (2008) of the *F14* SSM/I seems anomalous and is marked red in the figures. Those portions of the time series that are marked red are excluded when computing the offset and drift.

Remarkably, in no instance do we find any problems with TMI, which by all indications is an extremely stable sensor. The one caveat is that in this analysis we are looking at monthly averages, and problems associated with the emissive antenna tend to average out. The

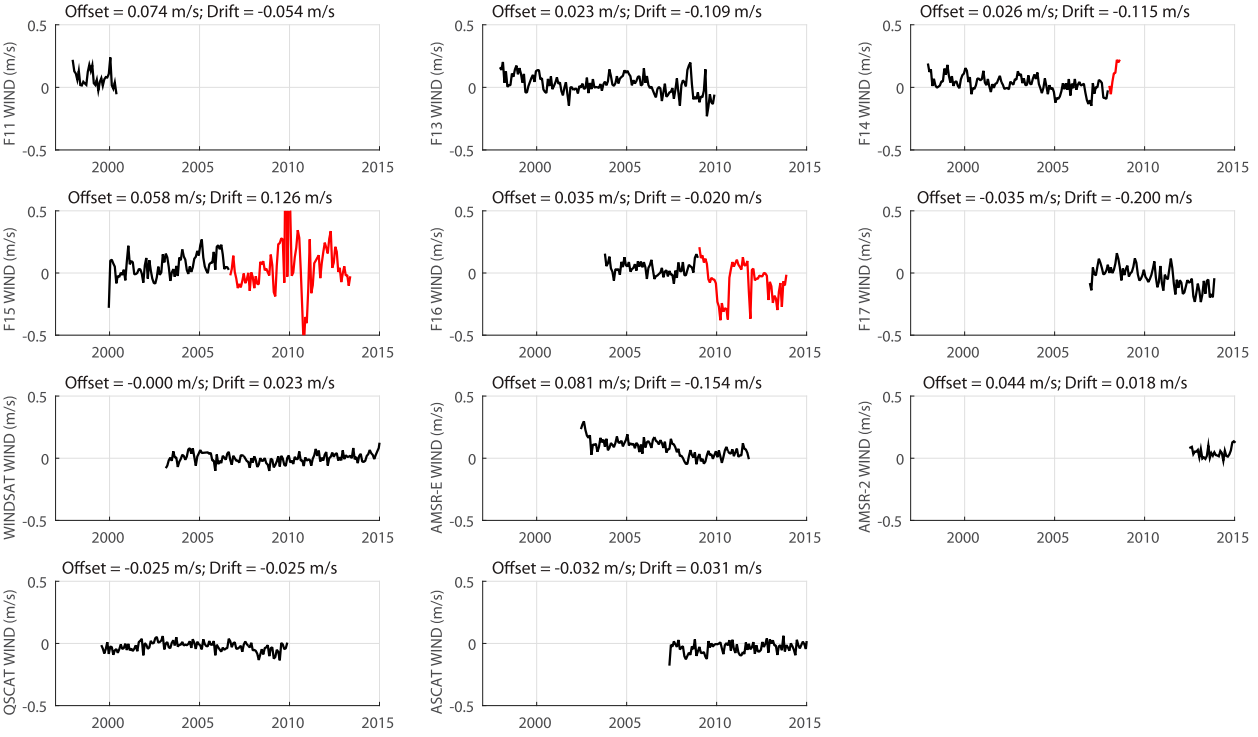

FIG. 11. Time series of monthly wind speed retrievals from nine MW imagers and two scatterometers compared to TMI. Red parts of time series represent problem periods for that particular sensor.

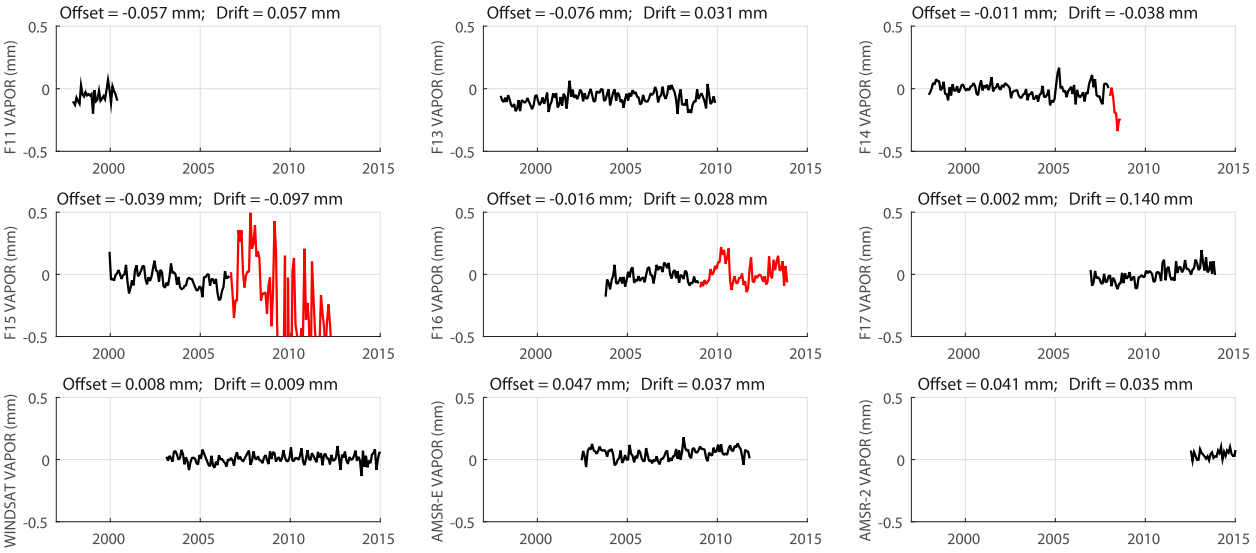

FIG. 12. Time series of monthly water vapor retrievals from nine MW imagers compared to TMI. Red parts of time series represent problem periods for that particular sensor.

comparisons of SST (Fig. 10) show excellent agreement as do the wind comparisons (Fig. 11) with the scatterometers and WindSat. Apart from the issues listed in Table 9, the vapor, cloud, and rain comparisons (Figs. 12–14) also look very good. There is no suggestion of a disconnect between the preboost TMI retrievals and the postboost retrievals (boost occurred August 2001). A close inspection reveals a very small upturn in the wind time series in 2014 for WindSat and AMSR-2 compared to TMI. We believe this is due to the rapidly decaying TRMM orbit that started in mid-2014. This change in altitude from 405 to 360 km is showing a spurious decrease the TMI wind retrievals of up to 0.05–0.1 m s^{-1}. However, the ASCAT comparison does not show this for some reason.

13. Validation using in situ observations

In this section we compare the TMI retrievals with in situ observations. These observations include SST, wind speed, and rain measurements from moored buoys as well as island GPS measurements of columnar water

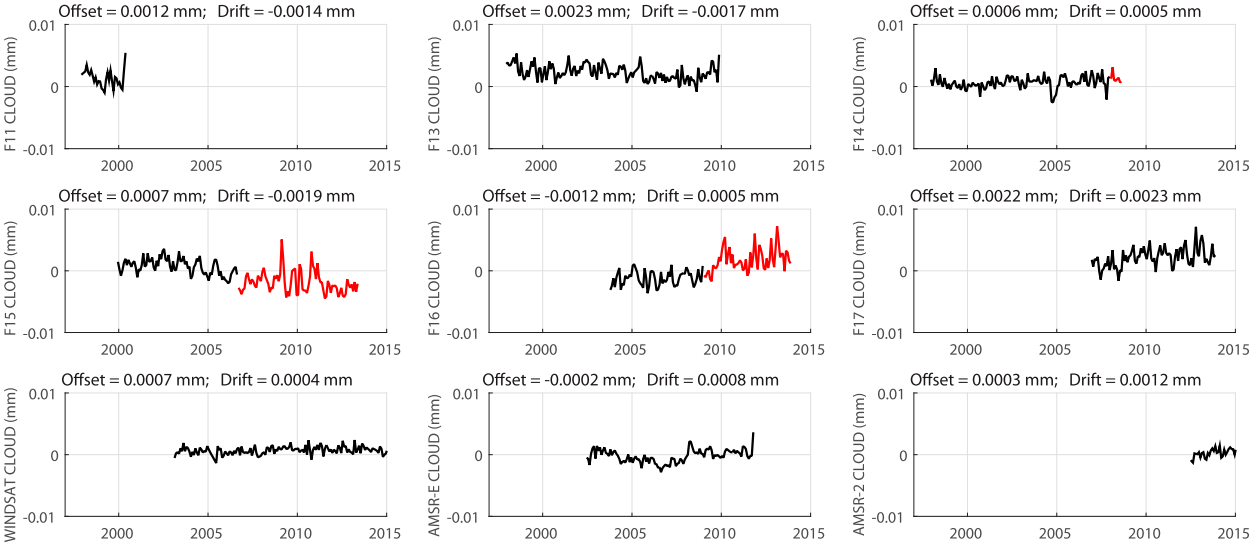

FIG. 13. Time series of monthly cloud water retrievals from nine MW imagers compared to TMI. Red parts of time series represent problem periods for that particular sensor.

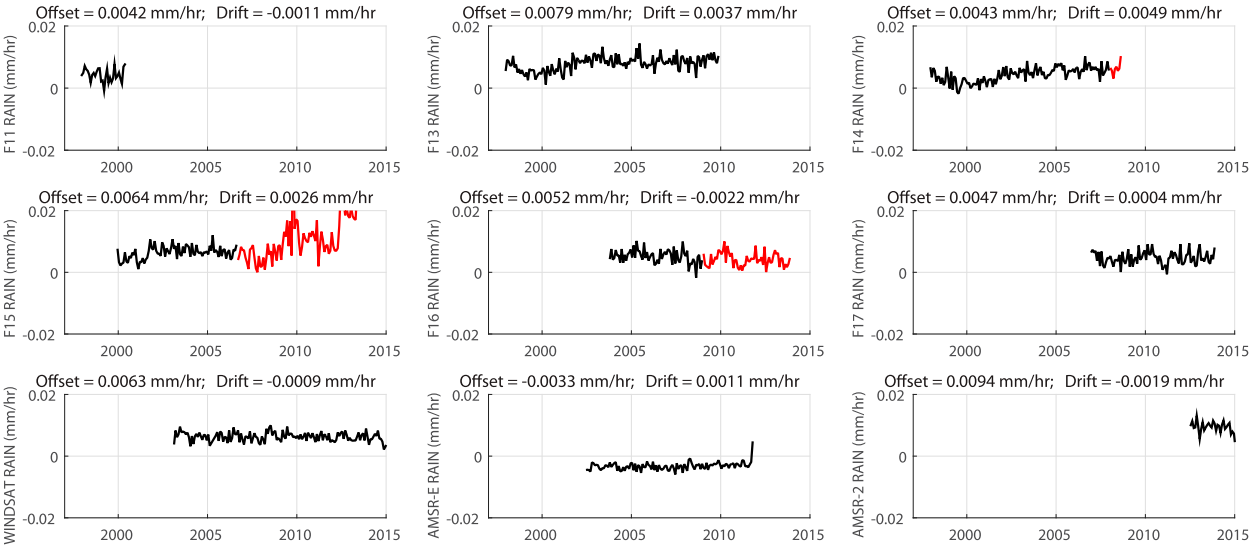

FIG. 14. Time series of monthly rain rate retrievals from nine MW imagers compared to TMI. Red parts of time series represent problem periods for that particular sensor.

vapor (Wang et al. 2007). The moored buoys include those operated by National Buoy Data Center (NBDC; Gower 2002; Portmann 2009) and by the Pacific Marine Environmental Laboratory (PMEL; McPhaden et al. 1998, 2009; Bourles et al. 2008). In addition to moored buoys, SST comparisons also include drifting buoys. The method used for the GPS vapor comparisons is described by Mears et al. (2015).

None of these in situ measurements was directly used during the TMI calibration process and hence represent a withheld dataset. Of course, the *F13*, WindSat, and AMSR-E geophysical retrievals, which were used for the T_A calibration, have been validated against similar in situ observations. We can now see if the closure requirement (17) successfully translates the T_A calibration into a precise E_p calibration.

The TMI SSTs are compared with drifting and moored buoy data. At low wind speeds during the day, the skin surface temperature, which is measured by TMI, can be significantly different from the at-depth temperature recorded by the in situ instruments. To avoid this diurnal warming problem, daytime wind speeds below $6\,\mathrm{m\,s^{-1}}$ are excluded from the comparisons. Figure 15 shows the 17-yr time series of the TMI SST minus in situ SST. The red line in Fig. 15a is the mean moored buoy/drifter SST and the black line is the collocated TMI SST. The mean difference and the standard deviation between the two are shown in Fig. 15b. These results are extremely consistent over the 17 yr. The overall TMI minus in situ bias is nearly the same for day and night: −0.01° and +0.02°C, respectively. Given the fact that the SST retrieval is quite sensitive to the emissive antenna problem, this consistency in the day versus night SST bias is strong evidence that the emissive antenna is being modeled correctly. The SST differences are also plotted versus SST, *W*, *V*, and *L* (not shown) to verify the TMI retrievals have the proper dynamic range and no crosstalk with the other E_p.

The TMI wind speeds are compared with those from the NDBC and PMEL moored arrays. All buoy wind measurements are normalized to a height of 10 m above the surface. The collocation window is 30 min and 25 km, and the comparisons go from the beginning of the TMI mission up through 2011. We omit data after 2011 from the analysis because of reduced buoy data availability.

TABLE 9. Problems identified by comparing the set of MW imagers with TMI.

Sensor	Problems
TMI	None
F11	Small offsets in *W*, *V*, *L*, and *R*.
F13	Drift of $-0.11\,\mathrm{m\,s^{-1}}$ in *W*; small offsets in *V*, *L*, and *R*.
F14	Drift of $-0.11\,\mathrm{m\,s^{-1}}$ in *W*; small offset in *R*; problem in last year of mission.
F15	Noisy retrievals after July 2006 due to RADCAL.
F16	After 2009: problems with *W*, *V*, and *L*.
F17	Drift of $-0.20\,\mathrm{m\,s^{-1}}$, 0.14 mm, and 0.002 mm in *W*, *V*, and *L*, respectively.
WindSat	Offset of $0.008\,\mathrm{mm\,h^{-1}}$ in *R*
AMSR-E	A transition near the beginning of 2008
AMSR-2	Offset of $0.01\,\mathrm{mm\,h^{-1}}$ in *R*
QuikScat	None
ASCAT	None

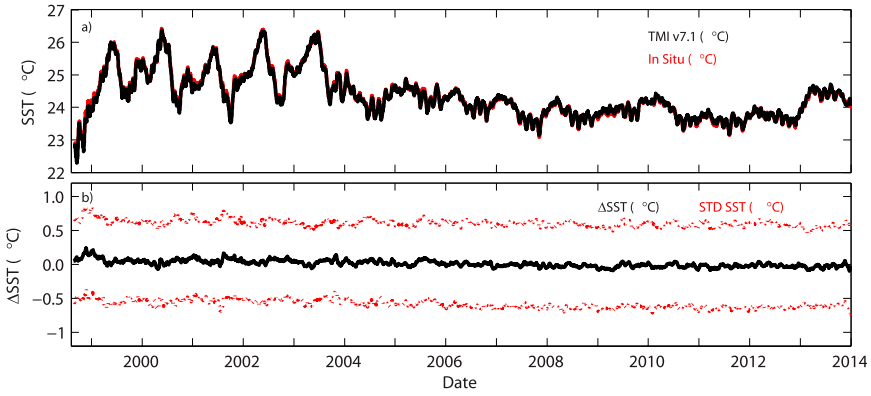

FIG. 15. (a) TMI SST retrievals (black) and ocean buoy and drifter measurements (red). (b) TMI minus in situ mean difference and standard deviation envelope. Overall bias and standard deviation is 0.01° and 0.61°C, respectively, for 496 341 comparisons over 17 yr.

Figure 16 shows the wind difference plotted versus mean wind speed. There are few buoy observations above 15 m s^{-1}, and at these higher winds the buoys tend to underestimate the winds (Howden et al. 2008). The wind speed differences are also plotted versus SST, V, and L (not shown) to verify the TMI retrievals have no crosstalk with the other E_p.

The TMI vapor retrievals are compared to those from GPS stations located on small remote islands. For this analysis, a 5 × 5 gridcell box is centered on the location of the GPS station and a local gradient is removed from the satellite field before comparison, as described by Mears et al. (2015). The comparison consisted of over 67 000 collocations for 26 stations. Figure 17 shows a scatterplot of the TMI vapor retrievals versus the GPS values. The overall mean difference of TMI minus GPS is 0.45 mm, which is large enough to be of some concern. We examined the GPS results for WindSat and found a similar bias. The original absolute calibration of the vapor retrieval was based on radiosonde comparisons (Wentz 1997) and now we see an inconsistency relative to GPS. Both radiosondes and GPS measurements are subject to their own particular bias problems, and we need to study this issue better to determine what the absolute vapor reference should be.

Figure 18 shows a scatterplot comparing collocated TMI rain rate retrievals with daily rain rates from PMEL tropical buoys located between 25°S and 21°N, with most of the buoys being within 10° of the equator. In the figure, each point represents a particular buoy for which the rain rates have been averaged over all time. We require a minimum record length of one year, which provides 78 buoys. There are a total of 238 924 individual collocations. Averaging over all buoys and all times gives a TMI value of 1576 mm yr^{-1} and a buoy value of 1572 mm yr^{-1}. This 4 mm yr^{-1} difference is remarkably small. The standard deviation of the 78 individual buoys in Fig. 18 is 287 mm yr^{-1} (18.3%), and the linear slope is 0.969 with an R^2 correlation of 0.936.

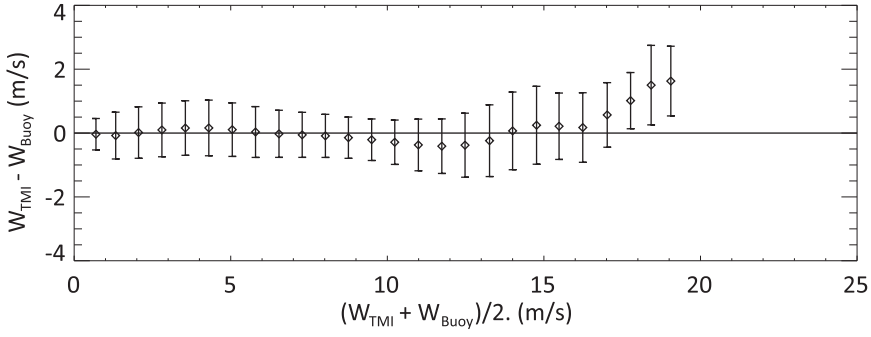

FIG. 16. A comparison of the TMI wind speed retrievals with ocean buoy measurements. For each 0.75 m s^{-1} wind speed bin, the mean and standard deviation are shown. The overall bias is −0.03 m s^{-1} and the overall standard deviation is 0.77 m s^{-1} for 258 642 comparisons over 14 yr.

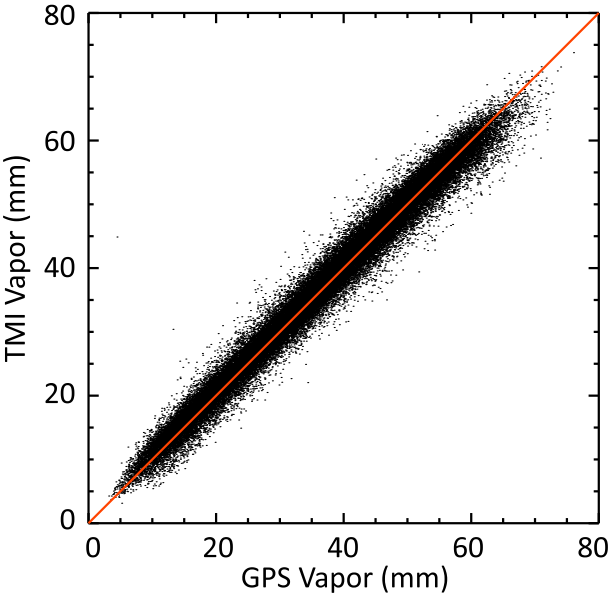

FIG. 17. A comparison of the TMI water vapor with GPS measurements of columnar water vapor. The overall mean difference (TMI minus GPS) is 0.45 mm and the standard deviation is 2.07 mm.

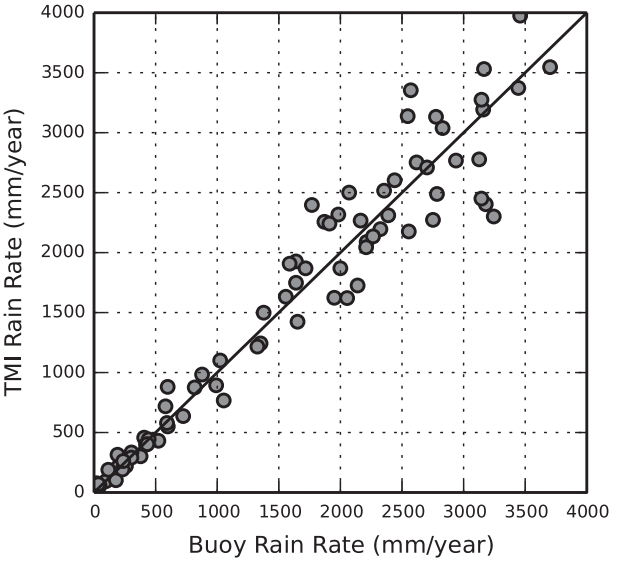

FIG. 18. A comparison of the TMI rain rate retrieval with ocean buoy rain gauge measurements. Each point represents a particular buoy for which the rain rates have been averaged over all time.

14. Trends from TMI

Figure 19 shows trend maps for the five TMI environmental parameters. These trends are found from a linear least squares fit of the E_p over the 17 yr of data with the seasonal cycle being removed. Trends are found for every 2° latitude–longitude cells from 40°S to 40°N. It should be emphasized that these trends are specific to

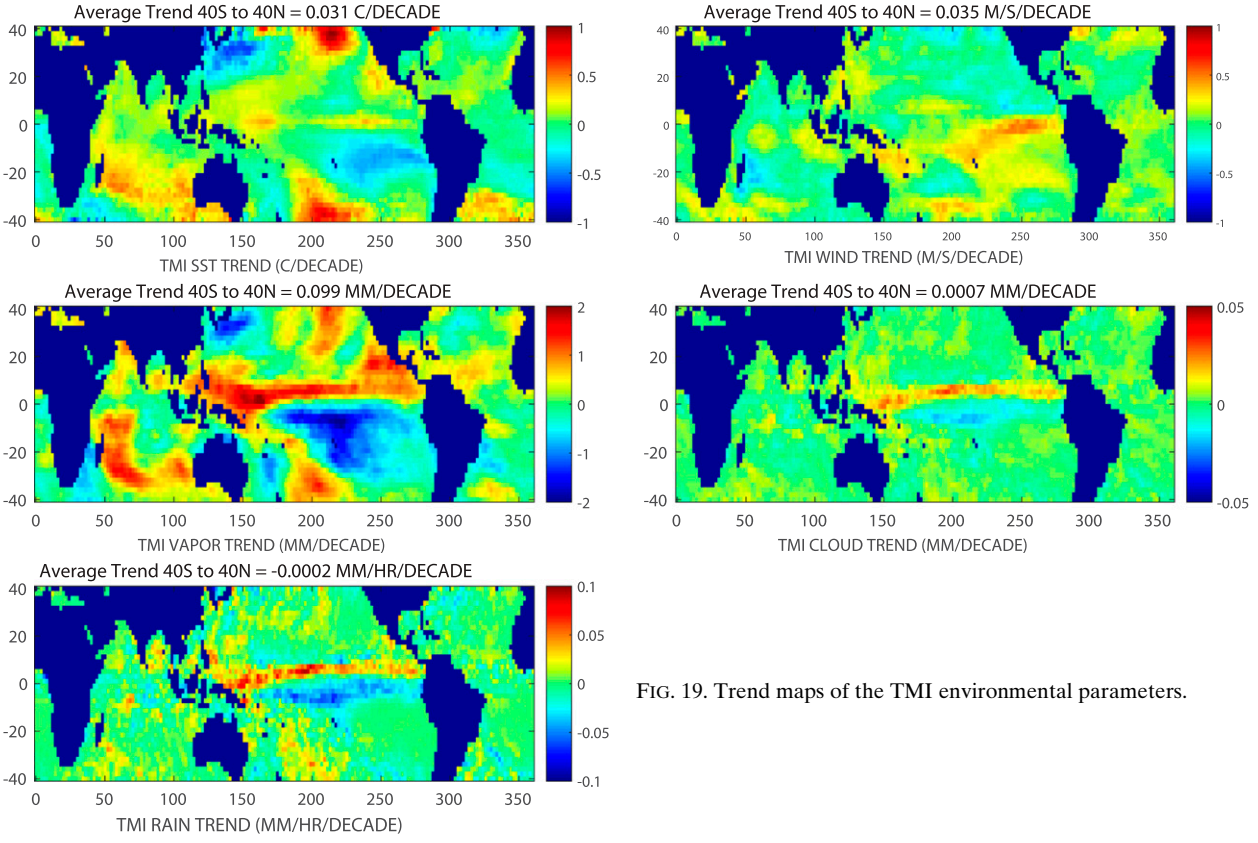

FIG. 19. Trend maps of the TMI environmental parameters.

TABLE 10. Summary statistics of intersatellite drifts and in situ comparison.

Parameter	Intersatellite drifts mean	Intersatellite drifts std dev	In situ differences mean	In situ differences std dev
SST (°C)	0.0165	0.0191	0.01	0.61
Wind speed ($m\,s^{-1}$)	−0.0279	0.0792	−0.03	0.77
Water vapor (mm)	0.0076	0.0475	0.45	2.07
Cloud water (mm)	−0.0002	0.0012	n/a	n/a
Rain rate ($mm\,h^{-1}$)	0.0008	0.0025	0.0005	0.0327

the TMI period of operation (1998–2014), and 1998 was the warmest year of the last century (Trenberth and Fasullo 2013; Trenberth et al. 2014). The displayed trends consist of a cyclic component associated with various climate oscillations [e.g., ENSO, the Pacific decadal oscillation (PDO), and the Indian Ocean dipole (IOD)] and an underlying component associated with long-term climate change. The separation of the two components is a major challenge for climate research. One obvious feature that does occur during the 1998–2014 period is a substantial moistening of the intertropical convergence zone accompanied by a drying in the tropical South Pacific. Although the regional trends can be quite large, the globally average trends (40°S–40°N, oceans only), which are given in Fig. 19, are small.

15. Conclusions

TMI is a very stable sensor as evidenced by comparisons with many other MW sensors. Table 10 gives a summary of these intersatellite relative drifts, where *F17* has been excluded because of an obvious drift problem. The table lists the mean and standard deviation of the drifts of the 10 sensors relative to TMI. In addition to demonstrating the stability of TMI, these comparisons also reveal obvious problems with some of the other sensors, most notably *F15* after the RADCAL was turned on, *F16* starting in 2009, and a persistent drift in *F17*. Also, AMSR-E may have a small shift that occurs around 2008. Table 10 also provides a summary of the TMI geophysical retrievals versus in situ comparisons. Close agreement is found with the exception of the 0.45-mm bias relative to the columnar vapor derived from GPS measurements. This bias is related to the difference between the GPS measurements and the radiosonde measurements used in the original calibration, and further study is required to resolve this difference.

The TMI T_B and E_p datasets, along with datasets from all the other MW sensors discussed here, are available from RSS. These datasets extend back to 1987 and provide nearly three decades of direct satellite observations of climate variability over the oceans. These observations should help clarify interannual and decadal climate oscillations, which will lead to building better climate indices.

Acknowledgments. This work was supported by NASA's Earth Science Division. The TMI 1B11 dataset used in this effort was made available by NASA's Science Mission Directorate, and are archived and distributed by the Goddard Earth Sciences (GES) Data and Information Services Center (DISC). We gratefully acknowledge the providers of data used to validate the TMI data: NOAA/PMEL TAO Project Office and the NOAA/National Data Buoy Center for moored buoy wind and rain data, NCDC for the Reynolds OI SST data, and Junhong Wang for GPS-derived TPW data.

REFERENCES

Bilanow, S., and S. Slojkowski, 2006: TRMM on-orbit performance reassessed after control change. *25th Int. Symp. on Space Technology and Science,* Kanazawa City, Japan, JAXA, ISTS 2006-d-35. [Available online at http://www.ai-solutions.com/Portals/0/AI%20Docs/Technical%20Paper%20Library%20pdf/2006/11.pdf.]

Bourles, B., and Coauthors, 2008: The PIRATA program: History, accomplishments, and future directions. *Bull. Amer. Meteor. Soc.,* **89,** 1111–1125, doi:10.1175/2008BAMS2462.1.

Brown, S. T., and C. S. Ruf, 2005: Determination of an Amazon hot reference target for the on-orbit calibration of microwave radiometers. *J. Atmos. Oceanic Technol.,* **22,** 1340–1352, doi:10.1175/JTECH1769.1.

Chelton, D. B., and F. J. Wentz, 2005: Global microwave satellite observations of sea surface temperature for numerical weather prediction and climate research. *Bull. Amer. Meteor. Soc.,* **86,** 1097–1115, doi:10.1175/BAMS-86-8-1097.

Draper, D. W., D. Newell, F. J. Wentz, S. Krimchansky, and G. Skofronick-Jackson, 2015: The Global Precipitation Measurement (GPM) Microwave Imager (GMI): Instrument overview and early on-orbit performance. *IEEE J. Sel. Top. Appl. Earth Obs. Remote Sens.,* doi:10.1109/JSTARS.2015.2403303, in press.

Gopalan, K., W. L. Jones, S. Biswas, S. Bilanow, T. Wilheit, and T. Kasparis, 2009: A time-varying radiometric bias correction for the TRMM microwave imager. *IEEE Trans. Geosci. Remote Sens.,* **47,** 3722–3730, doi:10.1109/TGRS.2009.2028882.

Gower, J. F. R., 2002: Temperature, wind, and wave climatologies, and trends from marine meteorological buoys in the northeast Pacific. *J. Climate,* **15,** 3709–3718, doi:10.1175/1520-0442(2002)015<3709:TWAWCA>2.0.CO;2.

Hilburn, K. A., 2009: Including temperature effects in the F15 RADCAL correction. Remote Sensing Systems Tech. Rep. 051209, 11 pp. [Available online at http://www.remss.com/papers/RSS_TR051209_RADCAL.pdf.]

——, and F. J. Wentz, 2008a: Intercalibrated passive microwave rain products from the Unified Microwave Ocean Retrieval Algorithm (UMORA). *J. Appl. Meteor. Climatol.,* **47,** 778–794, doi:10.1175/2007JAMC1635.1.

——, and ——, 2008b: Mitigating the impact of RADCAL beacon contamination on F15 SSM/I ocean retrievals. *Geophys. Res. Lett.,* **35,** L18806, doi:10.1029/2008GL034914.

Howden, S. D., D. Gilhousen, N. Guinasso, J. Walpert, M. Sturgeon, and L. Bender, 2008: Hurricane Katrina winds measured by a buoy mounted sonic anemometer. *J. Atmos. Oceanic Technol.,* **25,** 607–616, doi:10.1175/2007JTECHO518.1.

Kummerow, C., W. Barnes, T. Kozu, J. Shiue, and J. Simpson, 1998: The Tropical Rainfall Measuring Mission (TRMM) sensor package. *J. Atmos. Oceanic Technol.,* **15,** 809–817, doi:10.1175/1520-0426(1998)015<0809:TTRMMT>2.0.CO;2.

Kunkee, D. B., S. D. Swadley, G. A. Poe, Y. Hong, and M. F. Werner, 2008: Special Sensor Microwave Imager Sounder (SSMIS) radiometric calibration anomalies—Part I: Identification and characterization. *IEEE Trans. Geosci. Remote Sens.,* **46,** 1017–1033, doi:10.1109/TGRS.2008.917213.

McPhaden, M. J., and Coauthors, 1998: The Tropical Ocean–Global Atmosphere (TOGA) observing system: A decade of progress. *J. Geophys. Res.,* **103** (C7), 14 169–14 240, doi:10.1029/97JC02906.

——, and Coauthors, 2009: RAMA: The Research Moored Array for African–Asian–Australian Monsoon Analysis and Prediction. *Bull. Amer. Meteor. Soc.,* **90,** 459–480, doi:10.1175/2008BAMS2608.1.

Mears, C. A., B. D. Santer, F. J. Wentz, K. E. Taylor, and M. F. Wehner, 2007: Relationship between temperature and precipitable water changes over tropical oceans. *Geophys. Res. Lett.,* **34,** L24709, doi:10.1029/2007GL031936.

——, J. Wang, D. Smith, and F. J. Wentz, 2015: Intercomparison of total precipitable water measurements made by satellite-borne microwave radiometers and ground-based GPS instruments. *J. Geophys. Res. Atmos.,* **120,** 2492–2504, doi:10.1002/2014JD022694.

Meissner, T., and F. J. Wentz, 2010: Intercalibration of AMSR-E and WindSat brightness temperature measurements over land scenes. *IEEE Int. Geosci. and Remote Sensing Symp. 2010,* Honolulu, HI, Institute of Electrical and Electronics Engineers, doi:10.1109/IGARSS.2010.5649513.

——, and ——, 2012: The emissivity of the ocean surface between 6 - 90 GHz over a large range of wind speeds and Earth incidence angles. *IEEE Trans. Geosci. Remote Sens.,* **50,** 3004–3026, doi:10.1109/TGRS.2011.2179662.

Mo, T., 2007: Diurnal variation of the AMSU-A brightness temperatures over the Amazon rainforest. *IEEE Trans. Geosci. Remote Sens.,* **45,** 958–969, doi:10.1109/TGRS.2006.890417.

NASA, 2011: TRMM Microwave Imager (TMI) level 1 raw and calibrated radiance product (TRMM products 1B11). NASA/Goddard Earth Sciences Data and Information Services Center (GES DISC). Accessed daily 2011–15, version 7.002. [Available online at ftp://disc2.nascom.nasa.gov/data/s4pa/TRMM_L1/TRMM_1B11/.]

NCEP, 2000: NCEP FNL Operational Model Global Tropospheric Analyses, continuing from July 1999 (updated daily). National Model Archive and Distribution System, accessed 21 May 2015. [Available online at nomads.ncep.noaa.gov/pub/data/nccf/com/gfs/prod/.]

Portmann, H., 2009: Handbook of automated data quality control checks and procedures. National Buoy Data Center Tech. Doc. 09-02, 78 pp. [Available online at http://www.ndbc.noaa.gov/NDBCHandbookofAutomatedDataQualityControl2009.pdf.]

Precipitation Processing System, 2012: TRMM, file specification for TRMM products, version 7.002, NASA GSFC, 328 pp. [Available online at https://storm.pps.eosdis.nasa.gov/storm/data/docs/filespec.TRMM.V7.pdf.]

Reynolds, R. W., N. A. Rayner, T. M. Smith, D. C. Stokes, and W. Wang, 2002: An improved in situ and satellite SST analysis for climate. *J. Climate,* **15,** 1609–1625, doi:10.1175/1520-0442(2002)015<1609:AIISAS>2.0.CO;2.

——, T. M. Smith, C. Liu, D. B. Chelton, K. S. Casey, and M. G. Schlax, 2007a: NOAA Optimal Interpolation (OI) SST Analysis, version 2 (OISSTv2), continuing from 1981 (updated daily). National Climate Data Center Archive, accessed 21 May 2015. [Available online at ftp://eclipse.ncdc.noaa.gov/pub/OI-daily-v2/.]

——, ——, ——, ——, ——, and ——, 2007b: Daily high-resolution blended analyses for sea surface temperature. *J. Climate*, **20,** 5473–5496, doi:10.1175/2007JCLI1824.1.

Trenberth, K. E., and J. T. Fasullo, 2013: An apparent hiatus in global warming? *Earth's Future,* **1,** 19–32, doi:10.1002/2013EF000165.

——, ——, and L. Smith, 2005: Trends and variability in column-integrated atmospheric water vapor. *Climate Dyn.,* **24,** 741–758, doi:10.1007/s00382-005-0017-4.

——, ——, G. Branstator, and A. S. Phillips, 2014: Seasonal aspects of the recent pause in surface warming. *Nat. Climate Change,* **4,** 911–916, doi:10.1038/nclimate2341.

Wang, J., L. Zhang, A. Dai, T. Van Hove, and J. Van Baelen, 2007: A near-global, 2-hourly data set of atmospheric precipitable water from ground-based GPS measurements. *J. Geophys. Res.*, **112,** D11107, doi:10.1029/2006JD007529.

Wentz, F. J., 1997: A well calibrated ocean algorithm for Special Sensor Microwave/Imager. *J. Geophys. Res.,* **102** (C4), 8703–8718, doi:10.1029/96JC01751.

——, 2013: SSM/I version-7 calibration report. Remote Sensing Systems Tech. Rep. 011012, 46 pp. [Available online at http://images.remss.com/papers/tech_reports/2012_Wentz_011012_Version-7_SSMI_Calibration.pdf.]

——, and R. W. Spencer, 1998: SSM/I rain retrievals within a unified all-weather ocean algorithm. *J. Atmos. Sci.,* **55,** 1613–1627, doi:10.1175/1520-0469(1998)055<1613:SIRRWA>2.0.CO;2.

——, and M. Schabel, 2000: Precise climate monitoring using complementary satellite data sets. *Nature,* **403,** 414–416, doi:10.1038/35000184.

——, and T. Meissner, 2007: Supplement 1: Algorithm Theoretical Basis Document for AMSR-E Ocean Algorithms. Remote Sensing Systems Tech. Rep. 051707, 6 pp. [Available online at http://images.remss.com/papers/rsstech/2007_051707_Wentz_AMSR_Ocean_Algorithm_Version_2_Supplement1_ATBD.pdf.]

——, C. L. Gentemann, D. K. Smith, and D. B. Chelton, 2000: Satellite measurements of sea surface temperature through clouds. *Science,* **288,** 847–850, doi:10.1126/science.288.5467.847.

——, P. D. Ashcroft, and C. L. Gentemann, 2001: Post-launch calibration of the TRMM microwave imager. *IEEE Trans. Geosci. Remote Sens.,* **39,** 415–422, doi:10.1109/36.905249.

——, L. Ricciardulli, K. A. Hilburn, and C. A. Mears, 2007: How much more rain will global warming bring? *Science,* **317,** 233–235, doi:10.1126/science.1140746.

——, C. Gentemann, and K. Hilburn, 2015: TRMM TMI Daily Environmental Suite on 0.25° grid, version 7.1, Remote Sensing Systems. [Available online at http://www.remss.com/missions/tmi.]